JGR Space Physics

RESEARCH ARTICLE
10.1029/2024JA032910

EISCAT Observations of Depleted High-Latitude *F*-Region During an HSS/SIR-Driven Magnetic Storm

N. M. Ellahouny[1], A. T. Aikio[1], H. Vanhamäki[1], I. I. Virtanen[1], L. Cai[1], A. Marchaudon[2], P.-L. Blelly[2], A. Coster[3], J. Norberg[4], A. Maute[5], and S.-I. Oyama[6,7]

[1]Space Physics and Astronomy Research Unit, University of Oulu, Oulu, Finland, [2]Institut de Recherche en Astrophysique et Planétologie, Université de Toulouse, Toulouse, France, [3]Haystack Observatory, Massachusetts Institute of Technology, Westford, MA, USA, [4]Precursor-SPC, Finnish Meteorological Institute, Helsinki, Finland, [5]CIRES, NOAA/SWPC, University of Colorado at Boulder, Boulder, CO, USA, [6]Institute for Space-Earth Environmental Research, Nagoya University, Nagoya, Japan, [7]National Institute of Polar Research, Tachikawa, Japan

Abstract The effect of storms driven by solar wind high-speed streams (HSSs) on the high-latitude ionosphere is inadequately understood. We study the ionospheric *F*-region during a moderate magnetic storm on 14 March 2016 using the EISCAT Tromsø and Svalbard radar latitude scans. AMPERE field-aligned current (FAC) measurements are also utilized. Long-duration 5-day electron density depletions (20%–80%) are the dominant feature outside of precipitation-dominated midnight and morning sectors. Depletions are found in two major regions. In the afternoon to evening sector (12–21 magnetic local time, MLT) the depleted region is 10°–18° magnetic latitude (MLAT) in width, with the largest latitudinal extent 62°–80° MLAT in the afternoon. The second region is in the morning to pre-noon sector (04–10 MLT), where the depletion region occurs at 72°–80° MLAT within the auroral oval and extends to the polar cap. Using EISCAT ion temperature and ion velocity data, we show that local ion-frictional heating is observed roughly in 50% of the depleted regions with ion temperature increase by 200 K or more. For the rest of the depletions, we suggest that the mechanism is composition changes due to ion-neutral frictional heating transported by neutral winds. Even though depleted *F*-regions may occur within any of the large-scale FAC regions or outside of them, the downward FAC regions (R2 in the afternoon and evening, R0 in the afternoon, and R1 in the morning) are favored, suggesting that downward currents carried by upward moving ionospheric electrons may provide a small additional effect for depletion.

Plain Language Summary We study the effects of a moderate magnetic storm in March 2016 driven by solar wind high-speed streams in the high latitude ionosphere. The EISCAT incoherent scatter radar latitudinal scans in Tromsø, Northern Norway, and on Svalbard island are utilized together with other ground-based and satellite measurements. A strong, long-duration decrease in electron density at 290 km altitude is observed for the first 5 days of the storm in two distinct local time sectors. In the afternoon to evening local time sector, the depletion covers a broad range of latitudes from the polar cap to the subauroral latitudes, while in the morning to prenoon sector, it covers a smaller range of latitudes, mainly within the auroral oval and extends to the polar cap. We show that ion-neutral frictional heating due to strong plasma flows plays a major role in generating the depletion in the high-latitude ionosphere. Additionally, depleted regions favor the downward field-aligned current regions.

Key Points:

- Strong long-duration F-peak electron density decrease is seen by EISCAT radars for 5 days during a high-speed stream driven magnetic storm
- Depleted *F*-region covers a broad latitude range from polar cap to subauroral latitudes in the afternoon-evening magnetic local time sector
- Ion-neutral frictional heating is shown to play a crucial role in electron density depletion

Supporting Information:

Supporting Information may be found in the online version of this article.

Correspondence to:

N. M. Ellahouny,
Nada.ellahouny@oulu.fi

Citation:

Ellahouny, N. M., Aikio, A. T., Vanhamäki, H., Virtanen, I. I., Cai, L., Marchaudon, A., et al. (2024). EISCAT observations of depleted high-latitude *F*-region during an HSS/SIR-driven magnetic storm. *Journal of Geophysical Research: Space Physics*, *129*, e2024JA032910. https://doi.org/10.1029/2024JA032910

Received 27 MAY 2024
Accepted 29 AUG 2024

1. Introduction

During the declining phase of the solar cycle, solar wind high-speed streams (HSSs) that originate from solar coronal holes have a significant impact on geomagnetic activity (Denton & Borovsky, 2012; Gonzalez et al., 1999; Grandin et al., 2019; Tsurutani et al., 2006). When an HSS catches up with the preceding slow solar wind, it creates a compressed plasma region called the solar wind stream interaction region (SIR), also called as a corotating interaction region (CIR) when it can be observed during several solar rotations (Gosling & Pizzo, 1999; Kamide et al., 1998; Richardson, 2018). HSS/SIRs typically cause only weak to moderate geomagnetic storms (Dst ≥ -100 nT) (Tsurutani & Gonzalez, 1987), but the geomagnetic activity may last for several days (Borovsky & Denton, 2006) and have a prolonged effect on the ionosphere (Burns et al., 2012). During HSS/SIR-driven storms, chains of consecutive magnetospheric substorms arise (Tsurutani & Smith, 1979; Tsurutani et al., 2006) causing changes in ionospheric plasma convection (Bristow & Jensen, 2007; Clausen et al., 2013; Jayachandran et al., 2003) and currents (Pedersen et al., 2021). HSS/SIRs include large-amplitude Alfvén waves (Belcher &

Davis, 1971; Tsurutani et al., 1994), and for negative interplanetary magnetic field (IMF) B_z excursions they may generate a High-Intensity Long-Duration Continuous *AE* Activity (HILDCAA) event at high latitudes that may last for several days (Tsurutani & Gonzalez, 1987). HILDCAA intervals produce continuous energy injections and energetic particle precipitation into the polar upper atmosphere, leading to unusually long storm recovery phases (Tsurutani et al., 2004). This can modify the dynamics and chemical coupling processes of the ionosphere-thermosphere (I-T) system.

The effects of geomagnetic storms on the ionosphere are called ionospheric storms. Both positive and negative phases of ionospheric storms have been identified. A positive phase corresponds to an increase in the peak *F*-region electron density, while the negative phase corresponds to a decrease (Buonsanto, 1999; Prölss, 1997). The impact of moderate geomagnetic storms driven by HSS/CIRs on the ionosphere at mid-latitudes has been studied in several papers (Aa et al., 2021; Buresova et al., 2014; Denton et al., 2009; Emelyanov et al., 2023; Verkhoglyadova et al., 2013). Denton et al. (2009) reported a long-duration (more than 4 days) decrease in the peak *F*-region electron density. Burns et al. (2012) emphasized the important role of composition changes for mid-latitude negative storms. These storms may cause a prolonged impact on the ionosphere and heat the thermosphere by Joule heating and particle precipitation (Burns et al., 2012; Emelyanov et al., 2023; Turner et al., 2009) that leads to a global increase in neutral density at the upper *F*-region heights (Thayer et al., 2008).

Very few studies that focus on the effects of HSS/SIR-driven storms have been carried out for the high-latitude ionosphere, which has been studied more from the viewpoint of magnetospheric substorms with a duration of hours. A study of the effect of CIRs on auroral and polar latitudes was carried out by Sojka et al. (2009) during the International Polar Year using EISCAT Svalbard (ESR, 75.4°N MLAT), and Poker Flat (65.4°N MLAT) incoherent scatter (IS) radars. The study indicated that CIRs resulted in ionospheric heating as evidenced by the increase in ion temperature measured by the radars. Grandin et al. (2015) studied the effect of HSS/CIRs at auroral latitudes by making a superposed epoch analysis during HSS/CIRs between 2006 and 2008 using the Sodankylä ionosonde station (64.1°N MLAT). They found that the *F*-region critical frequency foF2, proportional to the peak electron density, decreased between 12 and 23 MLT in summer and around equinoxes for several days after the CIR impact. The physical processes for depletion discussed in the papers above include ion frictional heating and neutral composition changes in the *F*-region (see also Marchaudon et al., 2018), which will be discussed more in Section 4. Increases were observed in the morning sector and near noon, possibly associated with soft particle precipitation. Energetic (>30 keV) electron precipitation is also observed during 3–4 days after the CIR arrival at auroral and sub-auroral latitudes (Grandin et al., 2017).

Bjoland et al. (2021) made a statistical study to investigate electron density depletions in polar regions without addressing specifically HSS/SIR-driven storms. The study used several decades of Svalbard ESR radar measurements together with measurements from CHAMP and Swarm satellites. Ionospheric depleted regions were found in the early morning sector and were more prevalent during equinox and winter rather than summer for moderate or high solar activity. Bjoland et al. (2021) found the morning sector depletion regions were accompanied by ion temperature enhancements suggesting that ion frictional heating plays a role.

The goal of this paper is to characterize the high-latitude *F*-region response to a long-lasting HSS/SIR event with a focus on density depletions. The event took place during the equinox time on 14–19 March 2016. With the EISCAT Tromsø and Svalbard IS radars making meridian scan measurements, a large latitudinal region of 62°–80° MLAT in the *F*-region ionosphere is covered. The radars provide us with several plasma parameters, which help us to identify possible physical mechanisms behind the observed changes in the *F*-region electron density. We also utilize measurements of field-aligned currents by AMPERE and equivalent currents by IMAGE magnetometers, which helps to put the radar observations into the context of ionospheric boundaries. The paper is organized as follows. Data sources and data analysis are introduced in Section 2, and the results of data analysis are shown in Section 3. Section 4 discusses the possible physical mechanisms for the observed density depletions, and the conclusions are presented in Section 5.

2. Data and Analysis

2.1. Data Sources

2.1.1. EISCAT Data

In this study, the plasma parameters in the high-latitude ionosphere were measured by two EISCAT IS radars in northern Scandinavia. The coordinate system used in this study is the altitude-adjusted corrected geomagnetic (AACGM V2, Shepherd, 2014). The EISCAT data and other measurement are presented as functions of MLAT and MLT. The EISCAT UHF radar is located in Tromsø (66.6° MLAT, 102.9° magnetic longitude (MLON)), and the EISCAT Svalbard radar is located in Svalbard (75.4° MLAT, 110.7° MLON). During the storm event, the UHF and ESR radars were operated simultaneously with the Common Program CP3 experiment from 10 UT on 14 March 2016 to 14 UT on 19 March 2016. A CP3 experiment is designed to have meridional scans so that the measurements can yield the latitudinal distributions of the plasma parameters. The Tromsø UHF radar covered a latitudinal range of 62–72° MLAT, while the ESR radar covered a latitudinal range of 72–80° MLATs in the *F*-region at an altitude of 290 km. The meridional scans will be discussed more in Section 2.2.1. Both CP3 scans yield electron density, electron and ion temperatures, and line-of-sight ion velocity as a function of altitude and latitude. The line-of-sight ion velocity measurements are used to estimate the ion velocity vectors as will be described in Section 2.2.1.

2.1.2. Other Data Sources

Solar wind 1-hr average data propagated to the Earth's bow shock and magnetic indices (King & Papitashvili, 2005) have been taken from the OMNI 2 database https://omniweb.gsfc.nasa.gov/html/ow_data.html, and those will be shown in Section 3.1.

The AMPERE project uses more than 70 Iridium communication satellites in a near-polar orbit at an altitude of about 780 km. It gives field-aligned current (FAC) densities at high latitudes from the fitted magnetic field perturbations (B. J. Anderson et al., 2000; P. C. Anderson et al., 2008). Values below 0.16 μA/m^2, which is three times the standard deviation of the quiet-time current, are set to zero as described in B. J. Anderson et al. (2014) and Pedersen et al. (2021). AMPERE FAC data products have 1 hr MLT and 1° MLAT resolution. The FAC values are interpolated to 105.5 MLON (between Tromsø and Svalbard), and the results will be presented in Section 3.4.

The IMAGE (International Monitor for Auroral Geomagnetic Effects) network of ground magnetometers that is maintained by 10 institutes from Finland, Germany, Norway, Poland, Russia, Sweden, Denmark, and Iceland. It has 53 magnetometers covering 51–82° geographic latitudes to monitor the ionospheric auroral electrojets (Kauristie et al., 1996). In this study, we show the local *IE* index, which is a local version of *AE* index deduced from selected IMAGE magnetometers (Tanskanen, 2009) between 50 and 75° MLAT in Section 3.1. Moreover, equivalent current is calculated using the Spherical Elementary Current Systems (SECS) analysis developed by Amm and Viljanen (1999) and Vanhamäki and Juusola (2020). The equivalent currents data has been taken between the two EISCAT radar's longitude covering 60–77° MLAT, as will be discussed in Section 3.4.

2.2. Data Analysis

2.2.1. Vector Ion Velocity Analysis

Both the Tromsø UHF radar and the Svalbard radar were operated in the CP3 mode, in which the radar pointing direction is scanned along a magnetic meridian. In Tromsø, the scan starts from 23° elevation toward the north and moves through the zenith to 23° elevation toward the south in 15 discrete steps. The steps are approximately equidistant in MLAT, and the antenna makes a zigzag motion in azimuth so that the largest longitude separation in beam positions is about 3° in the *F*-region. The dwell time in each direction is approximately 1 min and the entire scan takes 24 min.

On Svalbard, the antenna moves continuously at a slow speed. The scan starts from 23° elevation toward the north, moves through zenith to 23° elevation toward the south within 12 min, and returns with the same speed so that the full scan takes 24 min. The antenna beam moves in azimuth so that the routes toward the south and toward the north cross in three points and the beam draws a “double eight” curve on the sky. The longitudinal width of the pattern is about 3° in the *F*-region.

In vector velocity analysis of the CP3 scans, data from a full 24-min cycle and from 200 to 400 km altitudes were binned in AACGM V2 coordinates. The bin width was 0.5° MLAT for the Tromsø UHF and the Svalbard ESR. Vector velocities were estimated using a least squares fit to all line-of-sight velocity measurements from each bin, assuming that the field-aligned velocity is zero. As data from different parts of the scan were used for individual vector velocity fits, the time resolution of fits varies from about 3 to 7 min for Tromsø UHF, and from 1.5 to 24 min for the ESR. As measurements along at least two different line-of-sight directions are needed for the vector velocity fit, data gaps are created at 65–68°MLAT around Tromsø, where most latitude bins are covered by only one line-of-sight direction in the *F*-region. The vector ion velocity data will be shown in Section 3.3.

2.2.2. Data Calibration and Quiet Day Background Determination

The IS radar electron density data always needs to be calibrated. For the Tromsø UHF radar, the dynasonde measurements have been used for calibration (Rietveld et al., 2008). Both the Tromsø and Svalbard radars carry out latitude scans and at an altitude of 290 km, there is a region of overlap between 72.25 and 72.75° MLAT. It was found that ESR data points showed somewhat smaller electron density values than TRO data within the overlapping region and hence a calibration was carried out for the ESR data with a coefficient of 1.29 to make the electron densities match.

Since the EISCAT data availability before the storm time is limited, we use the International Reference Ionosphere (IRI-2016) model (Bilitza, 2001; Bilitza et al., 2014, 2017) Fortran code to determine electron density (N_e) and ion temperature (T_i) background values for an altitude of 290 km. The day before the storm onset, 13 March 2016, was quiet with the Kp index $\leq 2^-$ and it has been chosen for the IRI run. The model inputs were set to fixed values as Ap (daily magnetic index) = 3, F10.7 (solar radio flux at 10.7 cm) = 91.5, IG12 (ionosonde-based IG index) = 37, and Rz12 (12-month running median of the solar sunspot number) = 50.4. The IRI model was used to calculate $N_{e,IRI}$ and $T_{i,IRI}$ values in a regular grid 1° MLAT for each UT hour at a fixed longitude 106° MLON corresponding to the radar scans. We additionally run the IRI model for two other heights at 210 and 370 km which will be used in Section 3.5. By comparing the background estimates from IRI with the available pre-storm EISCAT data on 14 March 2016 at 12–19 MLT, we found that the $T_{i,IRI}$ values required a correction factor 0.907, which is applied. No such correction was needed for $N_{e,IRI}$. After this, the $N_{e,IRI}$ and corrected $T_{i,IRI}$ values are used as baselines to calculate the change in electron density ΔN_e and ion temperature ΔT_i, shown in Sections 3.2 and 3.3.

3. Results

In this section, we discuss the geomagnetic storm during 14–19 March 2016 based on EISCAT observations, supported by other instruments. Because the start time for the EISCAT measurements was at 10 UT on 14 March 2016, the 24-hr periods starting at 10 UT will be referred to as D1 (14 March 10 UT–15 March 10 UT), D2 (15 March, 10 UT–16 March, 10 UT), D3 (16 March, 10 UT–17 March, 10 UT), D4 (17 March, 10 UT–18 March, 10 UT), and D5 (18 March, 10 UT–19 March, 10 UT).

3.1. Solar Wind as Driver

The solar wind and magnetic indices are presented in Figure 1 for 14–19 March 2016. The measured solar wind parameters, velocity V (panel a), as well as the IMF B_y and B_z GSM components, and the total magnetic field B_t (panel b) are shown with 1-hr average values from OMNI 2. The derived parameters are the solar wind dynamic pressure in panel c and the Akasofu ε parameter in panel d, which describes the solar wind energy input rate to the magnetosphere (Akasofu, 1981). Akasofu ε is calculated according to the following equation:

$$\varepsilon = \frac{4\pi}{\mu_o} V B_t^2 L_o^2 \sin^4\left(\frac{\theta}{2}\right), \quad (1)$$

where μ_0 is the vacuum permeability, $L_0 = 7\ R_E$ (R_E is the Earth's radius), and θ is the IMF clock angle given by

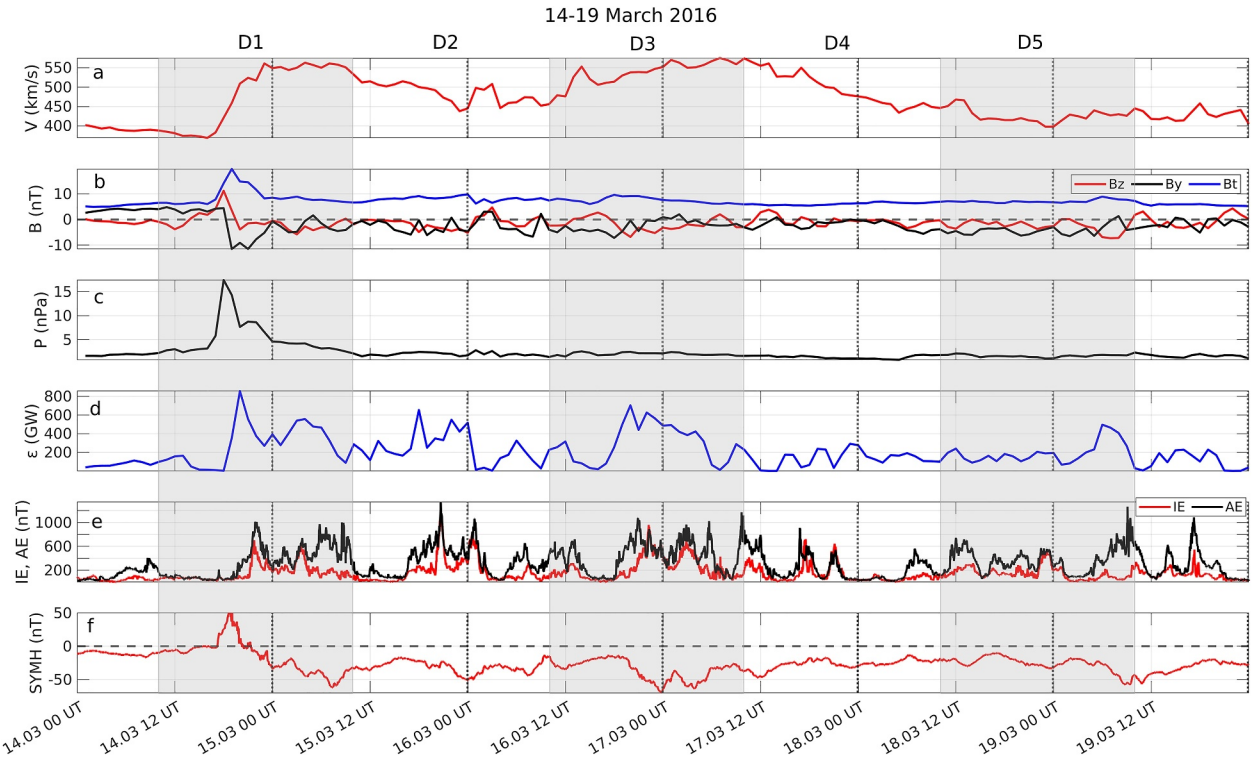

Figure 1. Overview of solar wind and geomagnetic indices for the 14 March 2016 storm. The parameters are as follows: (a) solar wind speed, (b) interplanetary magnetic field magnitude B_t, and B_y and B_z components in the geocentric solar magnetospheric coordinates (GSM), (c) solar wind dynamic pressure, (d) Akasofu ϵ parameter, (e) *AE* and *IE* indices, and (f) *SYM*−*H* index. The shaded/unshaded areas represent days in format D1–D5 as described in the text.

$$\theta = \begin{cases} \arctan\left|\frac{B_y}{B_z}\right| & \text{if } B_z > 0 \\ \pi - \arctan\left|\frac{B_y}{B_z}\right| & \text{if } B_z < 0 \end{cases} \quad (2)$$

The global and local auroral electrojet indices *AE* and *IE* are shown in panel e with 1 min and 10 s resolutions, respectively. The *SYM–H* 1-min index (Iyemori et al., 2010) for the ring current intensity is shown in panel f.

A moderate geomagnetic storm (-100 nT $\leq$ *SYM–H* ≤ -50 nT), as classified by Gonzalez et al. (1994) and Yokoyama and Kamide (1997), was driven by a solar wind HSS/SIR. The geomagnetic storm lasted 7 days and ended on 21 March when the *SYM–H* value became larger than -10 nT. A specific feature of this storm is that there were two maxima in solar wind speed, as will be discussed below, indicating that two HSSs interacted in this event, plausibly contributing to the long duration of the storm.

On D1, the slow solar wind with a velocity of 380 km/s increased to a peak velocity of 565 km/s (Figure 1a). The interaction between the fast and slow solar wind produced the compressed SIR plasma region, which can be identified on D1 from 17 UT to 23 UT with increases in the IMF magnitude reaching a maximum of 20 nT (panel b) and dynamic pressure with a peak of 17 nPa (panel c). The Akasofu ϵ exhibited a strong increase reaching 860 GW during the SIR (panel d). The storm's initial phase onset started at 17:20 UT as a positive increase in the geomagnetic *SYM*−*H* index reaching $+55$ nT (panel f) as a result of the dayside magnetospheric compression by the enhanced solar wind dynamic pressure. After the southward turning of the IMF B_z component with a minimum value of -9.4 nT at 20 UT, the onset of the storm main phase began on 14 March at about 21 UT when the *SYM*−*H* turned negative.

During the storm, the *SYM*−*H* index had four minima (one of them was a double structure) with values ≤ -50 nT. Therefore, the definition of the storm main phase using the minimum in *SYM*−*H* is not very well suited for this

event. The first minimum took place on D1, 15 March at 07:20 UT with a value of −62 nT. During the main phase on D1 before the first *SYM−H* minimum solar wind coupling was high (panel d), and consequently, the *AE* and *IE* indices reached values up 1,000 nT and 700 nT, respectively (panel e).

In the beginning of D2, the solar wind velocity was decreasing but the 1-hr IMF B_z remained negative. Akasofu ε reached 655 GW, and the *AE* and *IE* indices exceeded 1,200 nT. The *SYM−H* index exhibited the second minimum with −51 nT on 16 March at 00 UT.

The second HSS was observed on D3 with a peak velocity of 570 km/s, and the IMF B_z decreased to −7 nT during the velocity increase. That drove a wide peak in Akasofu ε with a maximum of 700 GW and increased *AE* and *IE* to 1,000 nT and 890 nT, respectively. During D3, *SYM−H* reached the third minimum with a value of −69 nT on 16 March at 23:50 UT, which was followed by a secondary minimum of −64 nT on 17 March at 03:50 UT.

During D4 and D5, the solar wind velocity returned gradually to lower values but the IMF B_z remained negative most of the time. The Akasofu ε was very small during D4, while the *AE* index had a few peaks reaching 600 nT in the first half of the day. In the latter part of D5, one more peak in the Akasofu ε parameter occurred due to a southward turning of the IMF B_z component, which produced the fourth minimum of −58 nT in the *SYM−H* index at the end of D5 on 19 March at 09:20 UT and strong increase in the *AE* index, but not in the local *IE* index.

3.2. Large-Scale Electron Density Behavior

The EISCAT data from the Tromsø and Svalbard radar scans have been combined in a single MLT-MLAT polar plot representation, showing the spatial and temporal behavior of the *F*-region plasma parameters at an altitude of 290 km. In the polar plots shown in Figure 2, the data are binned as follows. For Svalbard, the data are binned into a regular grid of 0.5° latitude. For Tromsø scans, the data are binned into a grid with a changing step size of 0.3°-0.9° MLAT, the shorter steps corresponding to beam positions with high elevation angle and the longer ones to beam positions with a low elevation angle.

Each horizontal pair of the polar plots in Figure 2 gives one 24-hr period of electron density N_e (left) and density deviation $\Delta N_e = N_e - N_{e,IRI}$ (right) from the IRI background at 290 km altitude. The IRI model was run with constant non-storm drivers. The day starts at 10 UT (the start time of the EISCAT experiment) corresponding to about 12 MLT marked by the black dashed line for all days. In each panel, UT is increasing counter clockwise, and therefore, for example, the continuation of D1 at prenoon 12 MLT is D2 postnoon after 12 MLT. Thus each panel has a discontinuity at 12 MLT. The terminator location is shown by the black line. The line has been composed by taking the terminator locations when the EISCAT scans intersect the terminator between 20:40 and 04:20 MLT at 290 km. The bottom-right polar plot panel gives the background $N_{e,IRI}$ described in Section 2.2.2. When discussing the depletion regions, we typically refer to regions where ΔN_e is decreased more than $5 \cdot 10^{10}$ m^{-3} from the background.

In Figure 2, D1 gives electron density conditions preceding the storm from 12 MLT (10 UT) to the initial phase onset at 19:20 MLT (17:20 UT). During that time, N_e (panel a) exhibits the ordinary dayside enhancement by the solar extreme ultraviolet (EUV) radiation between 12 and 19 MLT, as shown by comparing to the IRI model $N_{e,IRI}$. Superposed on that, there is an additional increase of electron density in the post-noon sector spanning a wide range of latitudes as seen in ΔN_e (panel b).

During D1 and D2, it is possible to identify an ionospheric trough. Troughs are called high-latitude or mid-latitude (main) troughs based on location, although it has been suggested that they may represent the same phenomenon (Voiculescu et al., 2010). The main ionospheric trough shows a prominent *F*-region electron density depletion, and it appears typically on field lines mapping to the plasmapause or plasmaspheric boundary layer and in the ionosphere close to the equatorward boundary of the auroral oval (Carpenter & Lemaire, 2004; Pierrard & Voiculescu, 2011). It spans a few degrees in latitude and is longitudinally elongated covering several hours of MLTs. The trough normally consists of three parts: an equatorward wall, a trough minimum, and a poleward wall (Yang et al., 2015). The trough minimum position has local time variation, it often occurs at higher latitudes in the afternoon, after which it migrates to lower latitudes during the dusk reaching its equator most position in the early morning sector (see Aa et al., 2020, and references therein). On D1, a quiet time trough starts to appear in ΔN_e (panel b) at 14 MLT with trough minimum at 76° MLAT, and moves to lower latitudes in the dusk sector reaching 62° MLAT at 22 MLT. Its width ranges between 1 and 5°. This is typical behavior of the *F*-region trough in the

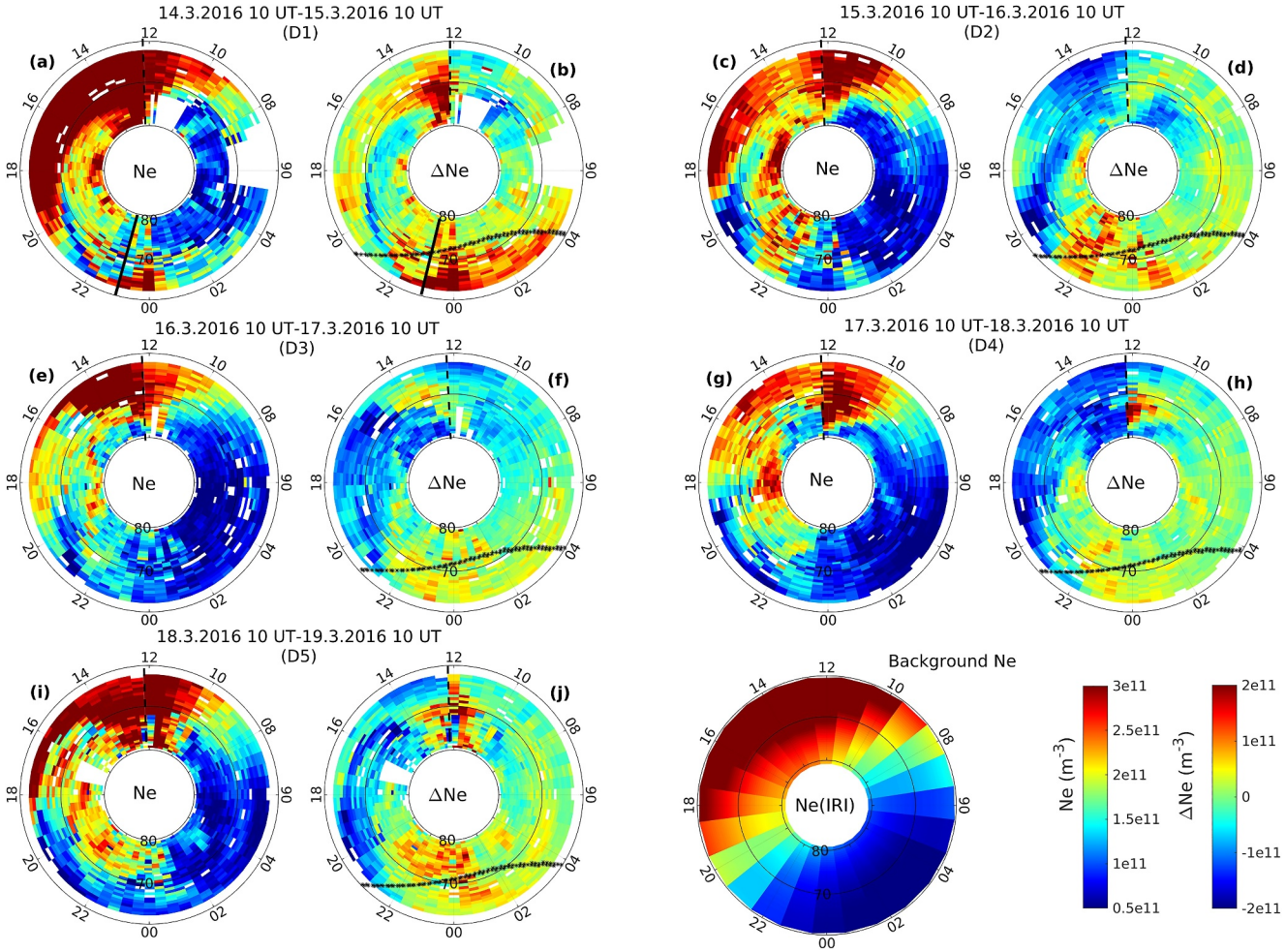

Figure 2. Polar plots of combined EISCAT Tromsø and Svalbard radar measurements from 14 March 2016 10 UT to 19 March 2016 10 UT (D1–D5) spanning latitudes 62–80° magnetic latitude (MLAT). In each panel, the electron density (N_e) is on the left and the change in N_e from the background (ΔN_e) is on the right, both at an altitude of 290 km near the *F*-region peak. The background N_e from the IRI model is shown in the lower right panel. The azimuthal coordinate is MLT, and the radial coordinate is MLAT. The black dashed line in each plot marks the start of measurements at 10 UT every day. The black solid line on D1 panels indicates the start time of the storm's main phase. On top of ΔN_e, the terminator location is shown in black. It has been composed by taking the terminator locations when the EISCAT scans intersect the terminator between about 20:40 and 04:20 MLT.

dusk sector as discussed above. As one can see from Figure 2, the IRI model produces smoothly varying background electron density in the *F*-region due to solar EUV, but it doesn't contain features like troughs, whose locations and intensities vary (Yang et al., 2015).

Following the storm's main phase onset at 23 MLT on D1, indicated by the solid black line, N_e and ΔN_e (panels a and b) experience strong increases due to particle precipitation as evidenced by simultaneous electron temperature enhancements (Figure S2 in Supporting Information S1) and formation of substorm electrojets as indicated by the *IE* and *AE* indices in Figure 1e. The N_e enhancements start at the lowest latitudes measured, but expand poleward to cover all latitudes around midnight MLT. In the post-midnight sector, enhancements in ΔN_e cover latitudes below 70° MLAT until 04 MLT. During morning hours, N_e has low values, but clear decreases in ΔN_e are seen at 08–12 MLT above 70° MLAT.

On D2, a notable decrease is seen in the dayside solar radiation-induced N_e (panel c), with ΔN_e (panel d) exhibiting a distinct depletion across all latitudes down to 62° MLAT at 12–16 MLT. Within approximately 71–77° MLAT we have a storm-time trough (Figure 2c), see also the discussion of enhanced ion velocities within the trough in Section 3.3. The trough minimum starts at about 75° MLAT at 13 MLT and moves equatorward to 62° MLAT at 21 MLT. This trough appears more pronounced and covers a broader range of latitudes in ΔN_e with a

width of 5–9° compared to the pre-storm trough observed on D1 (panel b). Many features on D2 are similar to D1, including the midnight particle precipitation effect and decrease in N_e during late morning hours, specifically at latitudes higher than 70° MLAT.

For D3–D5, the decrease in electron density is seen clearly in the afternoon to evening sector in ΔN_e (panels f, h, and j) during all these 3 days. The wide depletion region mostly exists at all measured latitudes covering 62–80° MLAT in the afternoon sector at 12–18 MLT, but recedes to a lower latitudinal range of 62–74° MLAT in the evening sector at 18–22 MLT.

Additionally, dayside *F*-region enhancements near noon can be seen in ΔN_e on many days. Some parts of them could be related to cusp. Those ΔN_e enhancements which extend to latitudes lower than the cusp may be associated with the formation of a tongue of ionization or polar cap patches (PCPs) (Foster et al., 2005). One mechanism to transport dense plasma from lower to higher latitudes is an equatorward expansion of ionospheric convection pattern and consequent poleward plasma flow (D. N. Anderson et al., 1988).

In the midnight sector for D3–D5, increases in ΔN_e (panels f, h, and j) are seen (weaker on D3 and D4 and stronger on D5). At oval latitudes we expect them to be associated with soft precipitation, but at higher latitudes, some of them can be identified as PCPs to be discussed in Section 3.4. From the morning to prenoon MLT sector at 04–11 MLT, the N_e indicates low values at all latitudes. ΔN_e (panels f, h, and j) presents depletion region primarily at higher latitudes above 70° MLAT except for D3 (panel f), where it covers latitudes down to 62° MLAT.

3.3. Role of Electric Field and Ion Temperature in Electron Density Depletion

Ion-neutral frictional heating caused by strong electric fields elevates the ion temperature and is one of the possible mechanisms causing *F*-region density depletions (Grandin et al., 2015; Rodger, 2008; Rodger et al., 1992; Schunk et al., 1976). Figure 3 left-hand side shows ΔN_e in percentage $((N_e - N_{e,IRI}) \cdot 100/N_{e,IRI})$, and on the right-hand side the ion temperature anomaly ΔT_i with respect to the background ion temperature $T_{i,IRI}$, both at 290 km altitude. The background $T_{i,IRI}$, shown on the right bottom panel, is calculated by using the IRI model as explained in Section 2.2.2. To emphasize regions with high ion velocities, only velocity vectors that exceed 600 m/s are shown on top of ΔT_i. When showing the depleted regions in Figure 3, we refer to the depleted ΔN_e with a decrease of more than 20% from the background.

We will first discuss the ionospheric trough characteristics seen on D1–D2 and associated ion temperature enhancements. On D1 in the afternoon to evening sector (Figure 3a), the quiet time trough is centered at about 76° MLAT at 14 MLT moving to lower latitudes and eventually to 62° MLAT at 22 MLT, after which it cannot be followed by EISCAT measurements. When the trough starts at 14–16 MLT at high latitudes, ΔT_i (panel b) indicates ion temperature enhancements of more than 200 K with large ion flows toward the dayside (Figure 3). The large-scale ion flow direction is typical for the two-cell convection pattern, where the plasma flows antisunward over the polar cap and sunward within the dusk and dawn auroral ovals. The flow intensity increases with the solar wind-magnetosphere coupling and specifically with negative IMF B_z component (Heppner & Maynard, 1987; Marchaudon et al., 2018; Ruohoniemi & Greenwald, 1996; Thomas & Shepherd, 2018). When the trough moves to lower latitudes after 18 MLT, it has no considerable ΔT_i or V_i increases.

On day D2, the storm time trough seen in ΔN_e (Figure 3c) is about 6–8° MLAT wide, much wider than on D1. The trough minimum is located at 74° MLAT at 14 MLT and it deepens when moving equatorward to reach 62° MLAT at 21 MLT. These features are in agreement with earlier studies, which have reported that the trough becomes deeper and shifts toward lower latitudes with increasing geomagnetic activity (Deminov & Shubin, 2018; Prölss, 2007; Shinbori et al., 2018; Yang et al., 2016). In the afternoon MLT, the trough minimum coincides with strong ion flows toward the dayside, and ΔT_i (panel d) is enhanced to exceed 300 K. As the trough deepens after 18 MLT, ΔT_i increases to more than 400 K. Many troughs are associated with increased ion temperature due to large electric fields (Rodger et al., 1992). However, this is not always the case, as for example, Voiculescu et al. (2010) reported a quiet-time trough, which rather showed ion temperature minimum than increase within the trough.

Second, we will discuss the afternoon-to-evening large-scale depletion regions in the *F*-region seen on D3–D5 in Figures 3e, 3g, and 3i. It is interesting to note that within this MLT sector Grandin et al. (2015) found a long-duration depletion around 64° MLAT during HSS/CIR-driven storms. On D2, only the storm-time trough

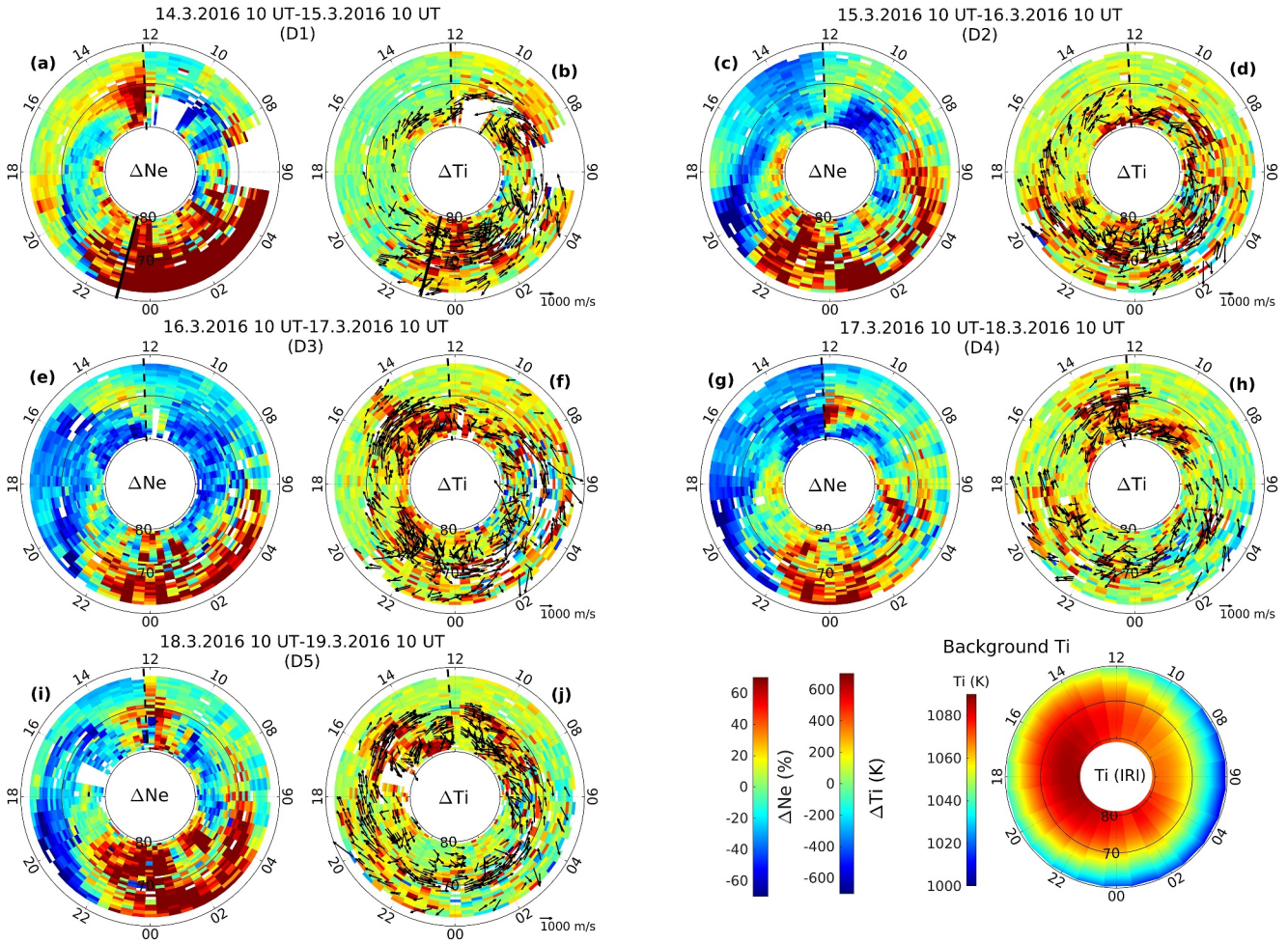

Figure 3. Same format as in Figure 2 but here the left panels show the change in electron density (ΔN_e) in percentage and the right panels show the change in the ion temperature (ΔT_i) from the background level (see details in the text). The vectors represent ion velocities that are greater than 600 m/s. The background T_i from the IRI model is shown in the right lower panel.

region (panel c) within 12–20 MLT is associated with elevated ΔT_i and large ion flows (panel d), while the ΔN_e depletion at 12–16 MLT equatorward of 70° MLAT doesn't show a significant ΔT_i increase. On each day D3–D5 (panels f, h, and j), there is a region of large increased ΔT_i reaching 350 K within the 12–16 MLT sector extending from the highest to the lowest latitudes (62–82° MLAT) and coinciding with depleted $\Delta N_e \leq -35\%$. At this afternoon sector within 68–73° MLAT (panels f, h, and j), there are strong sunward flows, while poleward of that, the strong flows are antisunward. However, there are large regions of depleted ΔN_e without increases in ion temperature, see for example, on D3 (panels e and f) 16–20 MLT at latitudes below about 70° and on D4 (panels g and h) at 15–18 MLT at all latitudes. On D4–D5 (panels h and j) at 18–22 MLT large sunward ion flows are again observed below 65° MLAT in connection with $\Delta N_e \leq -50$ % (panels g and i).

The third focus point is the morning-to-pre-noon depletion at 02–11 MLT, mainly at the higher latitudes. Figure 3 shows that for D1–D5 (panels a, c, e, g, and i), ΔN_e depletion $\leq -20\%$ covers 70–80° MLAT. On D3 (panel e), the depletion extends to cover all latitudes measured at 07–11 MLT. The depleted region above 70° MLAT on D1–D5 mostly coincides with T_i enhancements up to 300 K and high ion flow velocities (panels b, d, f, h, and j). Decreased ΔN_e at latitudes below 70° MLAT have no clear association with those features. The high-latitude depleted electron density characteristics match the observations reported by Bjoland et al. (2021). Using the EISCAT Svalbard radar data at 75.4° MLAT, Bjoland et al. (2021) detected regions of high latitude depletion in the post-midnight and morning sectors, which were associated with ion temperature elevation during the equinox season.

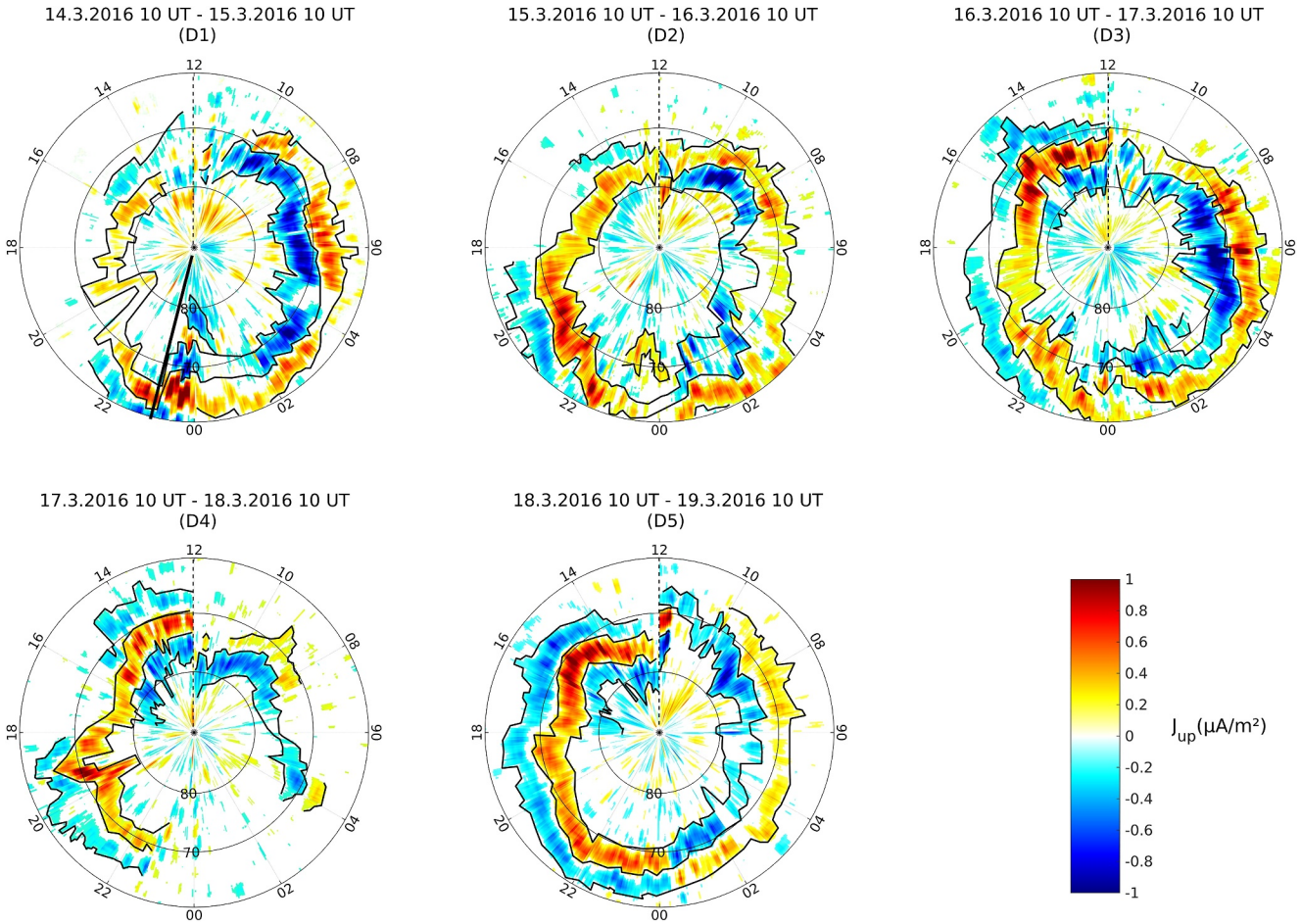

Figure 4. Keogram of AMPERE field-aligned current (FAC) at 105.5° MLON between Tromsø and Svalbard are presented for D1–D5 in MLT–MLAT coordinate system. Negative values are for downward FAC and positive values are for upward FAC. The black borderlines define the boundaries of FACs, and the dashed lines for the start of the day. The black solid line on D1 panel indicates the time of the storm's main phase.

3.4. Relationship of Electron Density Changes to Electrojets and FACs

In this section, we examine how electron density changes are related to the large-scale FAC regions, which connect the magnetosphere and the ionosphere electrodynamically (Cowley, 2000). The global FAC system consists of two current regions, Region 1 (R1) at higher latitudes and Region 2 (R2) at lower latitudes, and within the pre-midnight Harang discontinuity region both FACs can be observed. The poleward R1 FAC flows downward (upward) in the dawn (dusk) sector, while the equatorward R2 FAC has the opposite flow direction than R1 in the same sector (Iijima & Potemra, 1976, 1978). An additional current system may exist on the dayside poleward of R1 currents, known as Region 0 (R0) current (P. C. Anderson et al., 2008).

The keograms of FAC in Figure 4 are obtained by selecting the AMPERE FAC data from the magnetic longitude corresponding to the mid-plane (105.5° MLON) of the roughly meridional EISCAT scans for D1–D5. In Figure 4, the downward FAC is presented with negative values and the upward FAC has positive values. The gaps in the plot are due to very weak currents, as explained in Section 2.1.2. One such gap is seen on D4 at the midnight sector 23–03 MLT corresponding to 17 March 21 UT–18 March 01 UT during very low solar wind energy input (Figure 1d) and low *AE* and *IE* index values (Figure 1e). The intensity and location of large-scale FACs depend on the solar wind-magnetosphere coupling, which further depends for example, on the IMF direction and magnitude (P. C. Anderson et al., 2008; Iijima & Potemra, 1982; Juusola et al., 2014; Weimer, 2001). The black lines shown in the figure are based on a manual identification of the FAC boundaries.

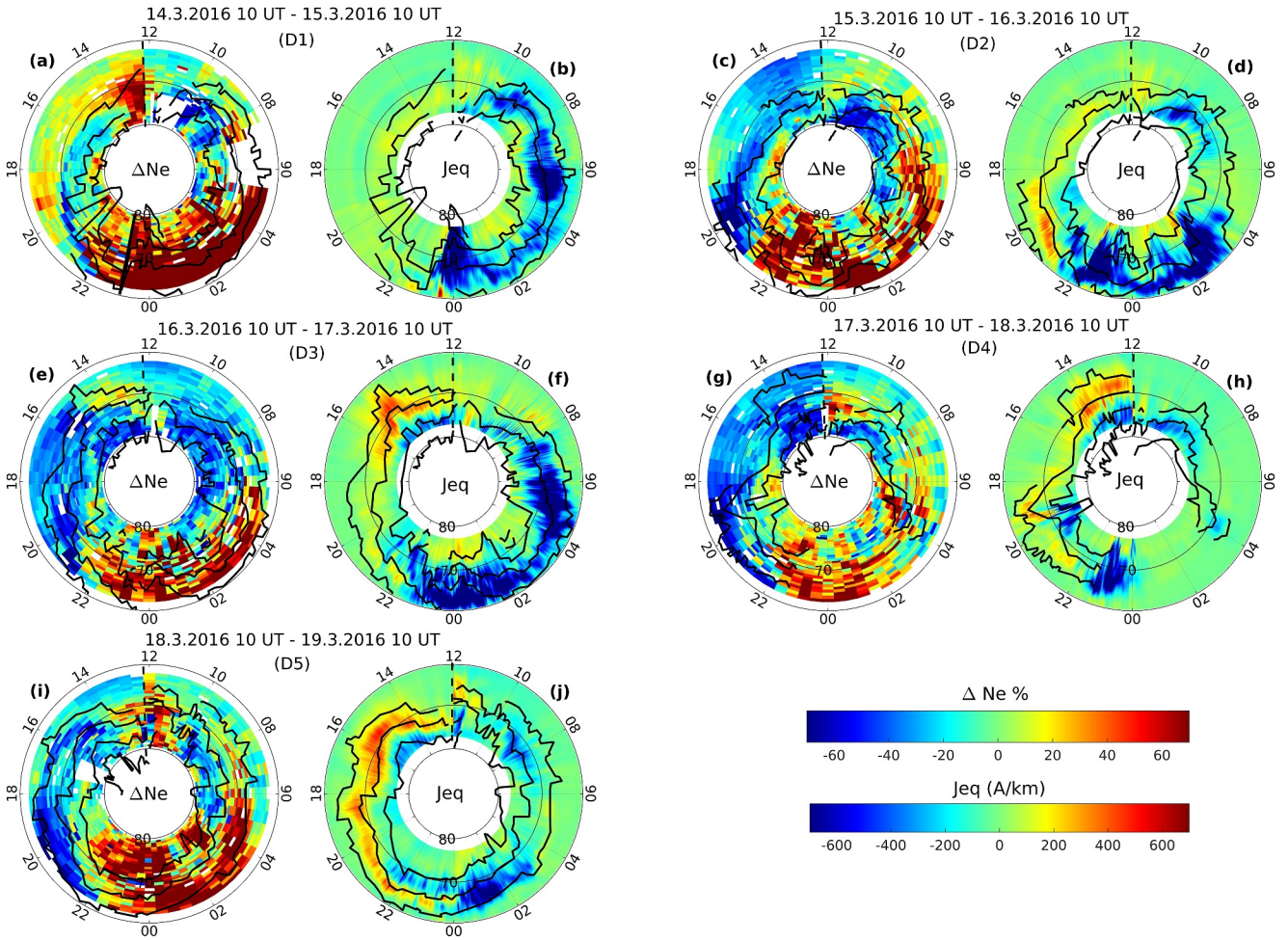

Figure 5. Same format as in Figure 3 with the left panels giving ΔN_e in percentage but the right panels show equivalent currents (J_{eq}) from IMAGE magnetometers network, positive values for eastward and negative values for westward currents. On top of them, black lines trace the boundaries of FACs from AMPERE as shown in Figure 4.

Before the storm onset, the FACs on D1 in Figure 4 show relatively low absolute values $\leq 0.4\ \mu A/m^2$, and the polar cap and the oval are very contracted until the storm main phase begins at 21 UT corresponding to 23 MLT shown by the black solid line in D1 Figure 4. Then, the polar cap widens so that the poleward boundary of the auroral oval moves to 66° MLAT, and the FAC intensity increases to 1 $\mu A/m^2$. The midnight sector shows multiple sheets of upward and downward FACs, typical for strong substorms. Enhanced R1 and R2 FACs exist in the morning sector until 10 MLT. Since the variations in FACs are related to the variations in horizontal currents, we will have a more detailed discussion of current dynamics in association with Figure 5. Three sheets of currents (R0, R1, and R2) emerge in the post-noon sector after 12 MLT on D3–D5, which is a typical feature for negative IMF B_y conditions as shown in Figure 1b, see for example, P. C. Anderson et al. (2008).

Figure 5 shows the electron density changes in percentage (left panel) along with the east-west component of equivalent currents J_{eq} (right panel) for D1–D5. Equivalent currents represent the divergence-free horizontal sheet currents, which often can be approximated as the Hall currents (Laundal et al., 2016). The black borderlines superposed on both panels display the boundaries of the FACs taken from Figure 4.

The J_{eq} is deduced from the IMAGE magnetometers network using the Spherical Elementary Current System (SECS) technique described by Amm and Viljanen (1999) and Vanhamäki and Juusola (2020). Values for the eastward electrojet (EEJ) are positive and for the westward electrojet (WEJ) negative in the figure. Previous studies have shown that EEJ flows in the afternoon-evening sector and WEJ in the morning-to-midnight sector

(Kamide & Vickrey, 1983). In the pre-midnight sector, the WEJ is located poleward of EEJ and the boundary between them defines the Harang discontinuity. Based on the day-to-day variations of FAC regions and J_{eq} intensity shown in Figure 5 for D1–D5, it is evident that the overall behavior of J_{eq} follows the general distribution of the FAC regions defined by the black boundaries. On the dusk side, the EEJ is observed under R2 FAC and partially under R1 current for D1–D5. On the dawn side, the WEJ lies under both R1 and R2 FAC regions. The R0 current in the post-noon sector seen on D3–D5 is associated with an extension of the WEJ from the pre-noon sector (panels f, h, and j).

Next, we will compare the current boundaries with the ΔN_e changes at different MLT sectors in Figure 5. In the magnetosphere, the R1 currents are believed to flow partly inside the boundary layer between the open and closed magnetic flux, while R2 current is believed to flow in the inner part of the plasma sheet and ring current region (Cowley, 2000). So, in the ionosphere, the peaks of R1 and R2 FACs are believed to be located within the auroral oval, while the poleward part of the R1 maps close to the polar cap boundary and the equatorward part of R2 maps close to the equatorward boundary of the auroral oval (Clausen et al., 2012).

We will first focus on electron density depletion regions. The pre-storm ionospheric trough on D1 (panel a) at 14–22 MLT is obviously located within the downward R2 FAC region, even though only the poleward boundary of R2 could be identified from the AMPERE data. The same applies to the storm time trough on D2 (panel c) at 14–21 MLT.

The second depletion region to be discussed is in the afternoon-to-evening sector. On D2 (panel c) at 12–15 MLT the depletion region extends to 62° MLAT. The depleted region between roughly 71–77° MLAT corresponds to the downward R2 current and flows within the storm-time trough region, as discussed in Section 3.3. The depleted region below 71° MLAT is located equatorward of the auroral oval and the ionospheric trough. On D3 (panel e) at 12–16 MLT, the depleted region is within the downward R0 and upward R1 regions, and at 16–21 MLT within the downward R2 and south of R2. On D4 (panel g) at 12–16 MLT all latitudes are depleted, containing R0, R1, R2 and south of R2 areas, but at 16–22 MLT, depletions are within R2 and south of R2. On D5 (panel i) at 14–17 MLT the depleted region covers R0, R1, R2, and south of R2, while at 17–22 MLT the deep depletion is located within the R2 downward current.

On D1 (panel a) at 8–10 MLT the depleted region occurs over the downward R1 region and poleward of it, the latter indicating polar cap region. At 4–8 MLT there are depletions both at R1 region and in a narrow region in the polar cap. On D2 (panel c) at 04–11 MLT the depleted region is mostly within R1, around 08 MLT also partly within the polar cap, and at 11 MLT also partly within the upward R2. On D3 (panel e) the morning depletion region covers regions poleward of R1, inside R1 and R2, and south of R2 at 06–12 MLT, so now the depletion has expanded to the south of the auroral oval. On D4 (panel g) the morning depleted region is contracted to cover only downward R1 at 07–12 MLT. On D5 (panel i) at 04–11 MLT depleted region covers R1 and poleward of R1.

Next, regions where the increase in ΔN_e is observed will be discussed. After the storm main phase onset on D1 (panel a) at 23 MLT marked with a black solid line, a series of substorms initiate, as can be seen in the *IE* index in Figure 1e. Substorms are seen as intensifications in the WEJ with a poleward expansion in the J_{eq} for example, at about 23, 05, and 09 MLT on D1 (panel b). This leads to particle precipitation which enhances ΔN_e (panel a) to 70% covering all the MLAT ranges around 00 MLT. The effect seen at *F*-region altitudes is a result of a soft component (≤1 keV) of the electron precipitation (Fang et al., 2010). Same kind of substorms effect in the midnight and early morning sectors are seen on other days D2–D5 (panels c, e, g and i) as well.

However, not all increases in ΔN_e are due to substorms and soft precipitation. Some of the increases take place poleward of the R1 current, indicating location within the polar cap. Further evidence that some ΔN_e enhancements occur within the polar cap is provided by electron temperature (T_e) measurements shown in Figure S2 in Supporting Information S1 (right panels). Auroral particle precipitation into the auroral oval increases the electron temperature there. Therefore, the boundary of increased electron temperature has proven to be a good indicator of the polar cap boundary in the dark hemisphere (Aikio et al., 2006; Østgaard et al., 2005). Figure S2 in Supporting Information S1 shows how the region of low T_e (< 1600 K) in the poleward part of the EISCAT scans between about 21 and 03 MLT is bounded by the poleward edge of the R1 current, both indicating the polar cap boundary. Increased ΔN_e within the polar cap can be seen on D2 (panel c) near 23 MLT, D3 (panel e) at 00–02 MLT, D4 (panel g) at 23 MLT, and perhaps most prominently on D5 (panel i) at 21–02 MLT. All these features occur within the region of low T_e and can be identified as PCPs, which are large-scale *F*-region dense plasma

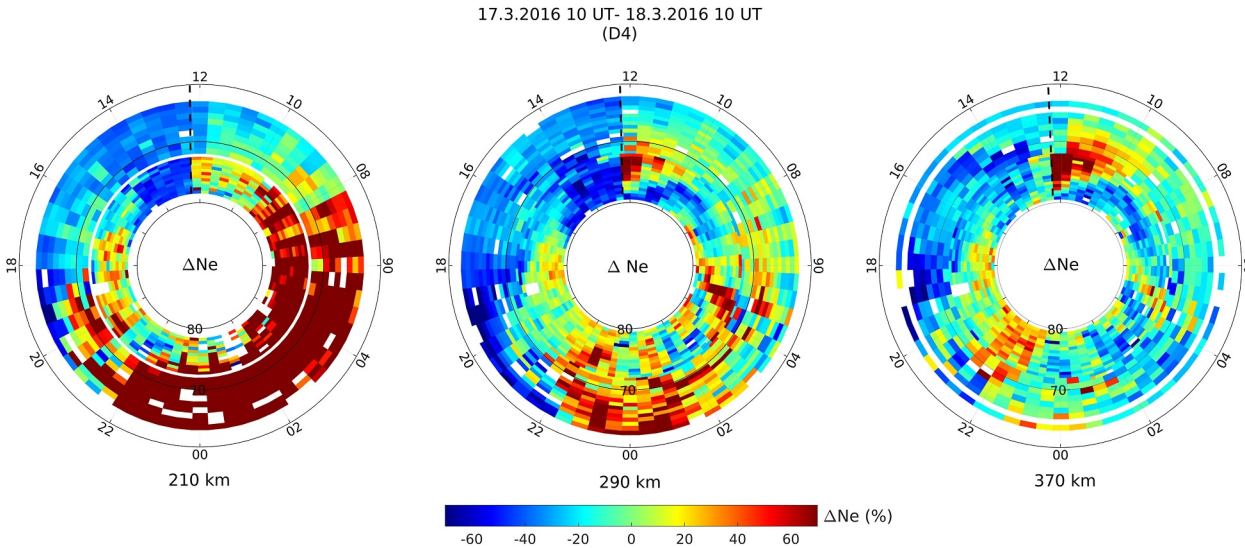

Figure 6. ΔN_e in percentage for D4 at different heights: 210, 290, and 370 km.

structures, extending from a few hundred kilometers to 1,000 km (Carlson, 2012; Crowley, 1996). The major source plasma of such patches is believed to be the solar EUV-induced ionization in the dayside mid-latitudes or subauroral region (Foster et al., 2005). The ionospheric convection driven by dayside reconnection transports the dense plasma from low to high latitudes (D. N. Anderson et al., 1988; Lockwood & Carlson, 1992; Moen et al., 2006). The dense plasma structures are segmented due to the temporal variation of convection to form PCPs (Hosokawa et al., 2019). After formation, PCPs are transported into the polar cap and further toward the nightside by ionospheric convection (Cai et al., 2024; Crowley, 1996).

3.5. Electron Density Changes at Different Altitudes

So far we have only shown ΔN_e from an altitude of 290 km (near the peak of the *F*-region) to discuss electron density depletions. To illustrate how electron density varies at different heights, Figure 6 shows an example of ΔN_e for D4 at altitudes of 210, 290, and 370 km. The altitude resolutions for the three altitudes are 15, 20, and 25 km, respectively. ΔN_e is calculated using the same procedure as explained in Section 2.2.2 using the IRI model to determine the background N_e for the selected heights.

In the afternoon to evening sector at 12–20 MLT, the large-scale density depletion ranging between 20% and 60% is seen at all altitudes extending from 210 to 370 km. However, at the altitude of 370 km, the depletion at 12–16 MLT is weaker than at the lower altitudes. At 210 km altitude, ΔN_e starts to show strong increases after 18 MLT, and after 20 MLT the increases cover all latitudes below 73° MLAT and exceed 70%. The ΔN_e enhancements continue throughout the night and morning sectors until 09 MLT. These increases are associated with particle precipitation and substorms. The energy spectra of precipitating electrons may have both the hard and soft components causing E- and lower *F*-region ionization, respectively.

The high-latitude (>70° MLAT) morning to pre-noon depletion region 06–12 MLT at 290 km is well visible also at 370 km, but not at 210 km. Besides, a notable decrease of ΔN_e over a wide range of 75–80° MLAT exists at 370 km in the early morning sector at 02–04 MLT, which is probably masked by soft precipitation effects at lower *F*-region altitudes.

The 370 km altitude shows two effects more clearly than the lower altitudes. One is an enhancement near 22 MLT above 70°, which is identified as a polar cap patch (it is located at latitudes higher than the R1 current poleward boundary). The other is the midday enhancement, whose origin is not entirely clear. Both these features are also seen at 290 km, but not well at 210 km altitude.

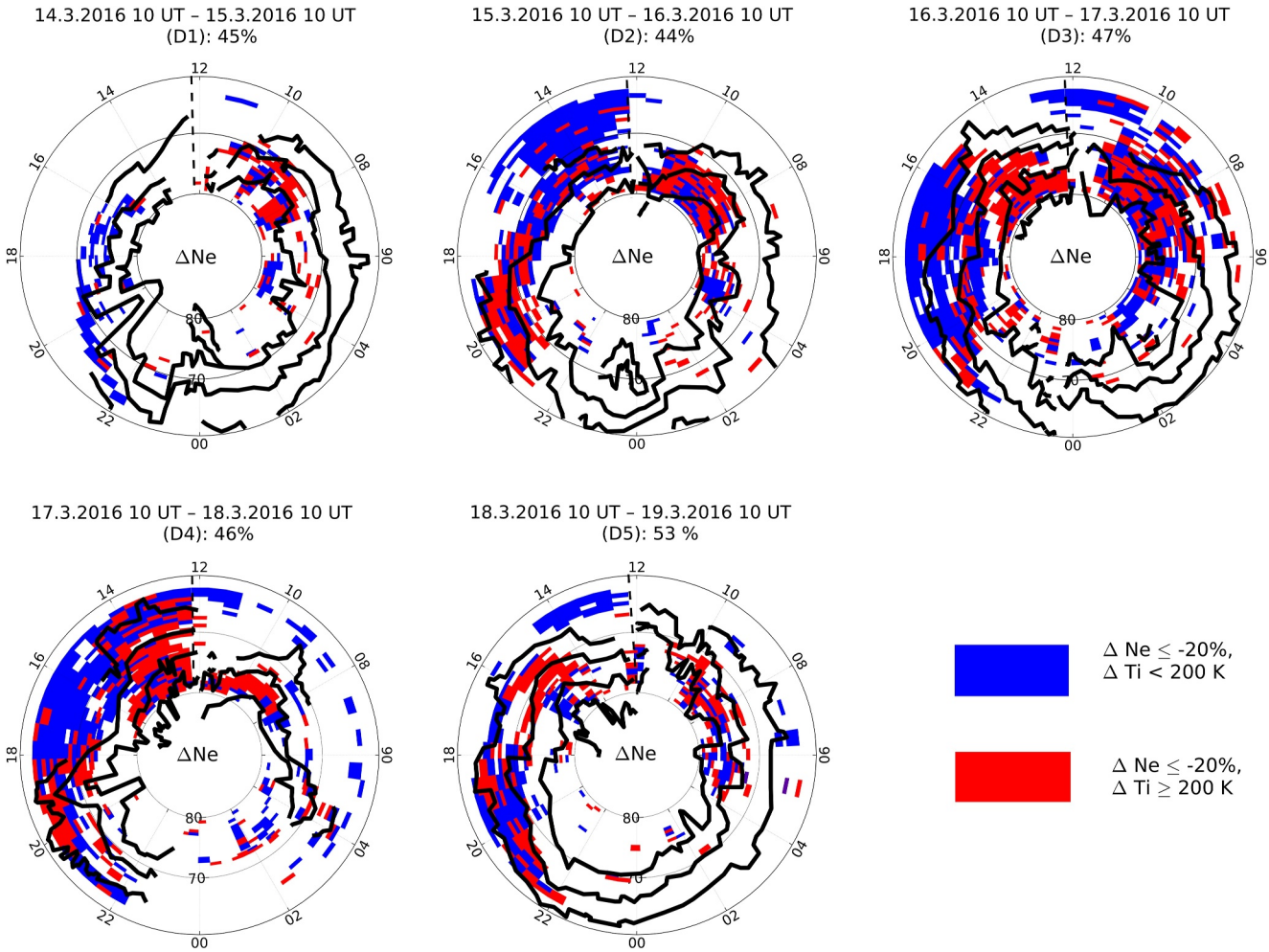

Figure 7. Locations of electron density depletions for days D1–D5 in the MLT–MLAT coordinate system. Blue regions correspond to $\Delta N_e \leq -20\%$ and $\Delta T_i < 200$ K and red regions to $\Delta N_e \leq -20\%$ and $\Delta T_i \geq 200$ K. The percentage in the title corresponds to the proportion of regions with ion temperature enhancements ≥ 200 K (red regions) of the total depleted regions (blue and red regions together). The field-aligned current region boundaries in black color are from Figure 4.

4. Discussion

4.1. Role of Ion-Neutral Frictional Heating in *F*-Region Electron Density Depletion

To study in more detail the role of ion frictional heating in the electron density depletion, we introduce Figure 7. It shows all regions where $\Delta N_e \leq -20$ % at 290 km altitude for D1–D5. The red color shows regions with ion temperature enhancement $\Delta T_i \geq 200$ K, while the blue color shows regions with $\Delta T_i < 200$ K. The FAC boundaries have been added as depicted in Figure 4 to see how the depletion regions match with R2, R1, and R0 FAC regions. The value 200 K was selected as the threshold since it is clearly larger than the nominal latitudinal variation in ΔT_i shown in Figure 3.

The proportion of regions with ion temperature enhancement >200 K (red regions) of the total depleted regions (blue and red regions together) for each day has been estimated, and we find the following values: D1 with 45%, D2 with 44%, D3 with 47%, D4 with 46%, and D5 with 53%. If we decrease the threshold value of ion temperature enhancement to 100 K, the range of values for D1–D5 increases to 60%–74%.

Hence, the results in Figure 7 show that typically about half of the significant electron density decreases ($\Delta N_e \leq -20\%$) are associated with local ion frictional heating with $\Delta T_i \geq 200$ K. As discussed in Section 3.3, those regions can be found on each day in the morning to pre-noon MLT sector at latitudes higher than 70° MLAT, except on D3, when the region reaches even lower latitudes. In the afternoon sector at 12–16 MLT it

covers a large MLAT range (D3–D5) and in the evening sector at 18–22 MLT, it locates within the R2 downward current. The other half of the depleted ΔN_e regions has no significant ΔT_i increase, and is often located at lower latitudes below 70° MLAT during the afternoon-evening. This means that some other mechanisms than local ion frictional heating should be involved to generate the observed electron density decreases.

The mechanism behind the electron density decrease in the *F*-region by ion frictional heating is well known (Rodger et al., 1992; Schunk et al., 1976) and briefly discussed below. The main *F*-region ion O^+ is produced by photoionization, but recombination of O^+ occurs via two-step processes with the two major molecules N_2 and O_2 as follows

$$O^+ + N_2 \xrightarrow{\kappa_1} NO^+ + N \quad \text{and} \quad NO^+ + e^- \xrightarrow{\alpha_1} N + O \tag{3}$$

$$O^+ + O_2 \xrightarrow{\kappa_2} O_2^+ + O \quad \text{and} \quad O_2^+ + e^- \xrightarrow{\alpha_2} O + O \tag{4}$$

The reaction rates κ_1, and κ_2 depend on the temperature of the O^+ ions. As NO^+ and O_2^+ rapidly recombine in the *F*-region, the speed of the recombination process is limited by the first processes of Equations 1 and 2. Therefore, the electron loss rate β is given by

$$\beta = \kappa_1(T_i)[N_2] + \kappa_2(T_i)[O_2] \tag{5}$$

where (N_2) and (O_2) are the number densities of the molecular nitrogen and oxygen. This equation shows two reasons for the electron density reduction. The first factor is the dependence of reaction coefficients on ion temperature. In specific, the reaction rate κ_1 becomes approximately proportional to the square of the ion temperature in high temperatures when $T_i > 1000$ K (Richards & Voglozin, 2011; Schunk & Nagy, 1980; St.-Maurice & Laneville, 1998). So, when there is a strong electric field in the ionosphere, the ion drift velocity increases, and due to ion-neutral frictional heating, T_i increases enhancing the recombination rate and reducing electron density. Zettergren and Semeter (2012) have shown with their electrodynamical model that, the conversion of *F*-region O^+ dominant plasma to molecular ions, and subsequent recombination at *F*-region altitudes according to the equations above may lead to depletion of electron densities in 2–5 min for strong auroral electric fields. The same effect was shown by Marchaudon et al. (2018) for an HSS-driven storm.

The second factor is due to the neutral densities (N_2) and (O_2) in Equation 3. Ion-neutral frictional heating in the thermosphere may drive upward vertical winds carrying molecular-rich air across pressure levels to higher altitudes (Forbes, 2007; Fuller-Rowell et al., 1994). That increases the recombination rate in the *F*-region and reduces electron density. This latter process is known as the thermospheric composition change in the *F*-region ionosphere (Burns et al., 1991; Fuller-Rowell et al., 1994; Marchaudon et al., 2018; Mayer et al., 1978; Prölss, 1997). Indeed, many studies utilizing satellite measurements and modeling have shown thermospheric reductions of column $[O/N_2]$ ratios during storm negative phases (Liu et al., 2012; Marchaudon et al., 2018; Meier et al., 2005; Zhang et al., 2004).

4.2. Other Processes Related to *F*-Region Electron Density Depletion

During storms, enhanced ion-neutral frictional heating (also called Joule heating) or particle precipitation may cause composition changes as discussed in the previous section. Neutrals are not affected by electric fields, but they can be carried away by neutral winds. Hence, if the fraction of neutral molecules has increased at a given location at *F*-region altitudes due to local ion-neutral frictional heating, thermospheric winds can carry the molecular-rich air to other regions, even to sub-auroral or middle latitudes. The effect of the composition change in the new location is to reduce electron density (Fuller-Rowell et al., 1994; Prölss, 1997). We suggest that many of the lower latitude regions marked in blue in Figure 7 are depleted because of composition change due to transport. Those regions are wide in latitude and are located at latitudes below the auroral oval. We also note that equatorward winds would be needed to transport the neutral composition change to lower latitudes on the dawn and dusk sectors, but unfortunately we have no wind measurements to support that conclusion. It is well known that equatorward winds can be generated on the nightside, specifically in the post-midnight sector during active conditions (Cai et al., 2019; Deng & Ridley, 2006; Oyama et al., 2023).

We also observe both the quiet-time trough (on D1) and the storm-time trough (on D2) in the dusk sector. The storm-time trough is clearly associated with enhanced ion velocities and elevated T_i, so ion-neutral frictional heating is a likely mechanism for the depletion. Very strong ion velocities can be found within the regions of subauroral ion drift (SAID, Spiro et al., 1979) or subauroral polarization stream (SAPS, Foster & Burke, 2002) just equatorward of the auroral oval. Indeed, Aa et al. (2021) found an intense SAPS of 1,000 m/s overlapping with a deepened main trough structure during a minor storm. We also observe a deepened trough on D2, and when it reaches latitudes below 64° MLAT near 20 MLT, the velocity vectors measured by EISCAT exceed 1,000 m/s as seen in Figure 3d.

The quiet-time trough is associated with ion-neutral frictional heating only in the afternoon as seen in Figures 3a and 3b, but not at later MLT times. The effect of frictional heating in sunlit ionosphere is discussed for example, by Voiculescu et al. (2016). One mechanism to produce a quiet-time ionospheric trough is the stagnation mechanism operating in the evening sector. It develops when the eastward plasma corotation nearly cancels the westward convection and plasma stays a long time (i.e., stagnates) in the darkness so that its density decreases due to the lack of solar EUV ionization (Nilsson et al., 2005; Rodger et al., 1992; Voiculescu et al., 2010). That mechanism is not plausible in our case for the quiet-time trough. We study an equinox event where the depleted regions are illuminated between 04 and 21 MLT, as can be seen from Figure 2, where the terminator location at 290 km altitude has been added as a black line. Also, it has been proposed that a possible mechanism explaining the formation of a sunlit trough is the transport of low-density plasma carried sunward from the nightside (Pryse et al., 1998; Rodger et al., 1992; Whalen, 1989).

In Figure 5 and Section 3.4 it was shown that in some regions depleted densities seem to coincide with downward FACs, namely in the post-noon (R0 current), in the afternoon-to-evening (R2 current), and morning-to-pre-noon (R1 current) sectors. The possibility of FACs affecting E- and *F*-region densities has been discussed in several papers. Mostly, the mechanism has been connected to relatively narrow regions of downward FACs producing the return currents for auroral arc current systems (Aikio et al., 2002; Marklund et al., 2001). The downward FAC carriers are thermal ionospheric electrons and both observations and simulations indicate that they may produce density cavities not only to the *E*-region but also extending also to the lower *F*-region (Aikio et al., 2004; Doe et al., 1993, 1995; Karlsson & Marklund, 1998; Zettergren et al., 2014). In this paper, the depleted regions are as wide as or wider than the R1 and R2 current regions. Nilsson et al. (2005) carried out modeling of trough dynamics and found that a current density typical of large-scale R2 FAC was enough to deepen the trough, when another mechanism (stagnation in their study) was affecting, too. The magnitude of electron density decrease depends on the magnitude of the FAC and on how long the evacuation of electrons by the FAC can affect the flux tubes. However, Zettergren and Semeter (2012) showed that conversion of *F*-region plasma to molecular ions and subsequent recombination was more important than current closure loss to produce plasma depletions in the 250–400 km altitude ranges. A possible scenario is that within the downward current regions, the ionospheric electric fields tend to be strong causing ion frictional heating and then the evacuation of *F*-region thermal electrons to carry the current causes a smaller additional effect. Indeed, if we look at Figures 5 and 7, most of the downward FAC regions are associated with ion temperature enhancements.

4.3. Role of HSS Driving

The main drivers for geomagnetic storms are interplanetary coronal mass ejections (ICMEs), which are gigantic magnetized plasma clouds launched into interplanetary space from the Sun (e.g., Kilpua et al., 2017) and HSS/SIRs. Most storm modeling efforts have focused on strong storms, often driven by ICME (e.g., Crowley et al., 2006; Pedatella, 2016; Pedatella & Liu, 2018), or driven by combined ICME and CIR drivers (e.g., Schmölter & Berdermann, 2021). A specific feature of the studied storm is that it is driven by two interacting HSSs and is just barely moderate in magnitude. The long duration of storms driven by HSS/SIR regions is a well-known feature. During the declining phase of Solar Cycle 23, the 9-day periodicity found in the occurrence of coronal hole features and associated HSS/CIR events has been studied a lot in terms of thermospheric mass density and composition (Crowley et al., 2008; Lei et al., 2008; Thayer et al., 2008).

Sojka et al. (2009) found by using observations from the Poker Flat and EISCAT Svalbard IS radars during HSSs that ion-neutral frictional heating at 300 km occurs on two distinct time scales: short period (in a few hours) that

increases T_i by many hundreds of degrees as well as a longer-term (in a few days) that increases T_i by about 100 K. They suggest that the longer period of heating, with a duration of days, will best relate to the thermospheric thermal state during the CIR events. The multiple-day heating events were present in both the auroral and polar cap regions.

In this study, we used a limit of 200 K for ΔT_i to characterize strong ion-neutral frictional heating regions, and those were found on each day during the storm, even though there were periods of less intense solar wind driving, for example, the period starting on D4 and extending to D5 on 17 March 12 UT–19 March 01 UT (see Akasofu ϵ in Figure 1d). During that period, nevertheless, substorm activity (as indicated by the *AE* index in Figure 1e) took place, and the *F*-region density depletions prevailed in the high-latitude region. Pedersen et al. (2022) showed that HSS-driven storms contain many substorms also in the late recovery phase, more than ICME-driven storms. The role of substorms during storm time is likely to be important in high-latitude forcing, producing continuous ion-neutral frictional heating and prolonged effects on the thermosphere.

5. Conclusions

Two interacting solar wind HSSs produced an unusually long-lasting moderate magnetic storm (minimum *SYM–H* = −69 nT) during spring equinox, which lasted for seven days. The high-latitude *F*-region has been studied during the HSS-driven storm using the EISCAT radars in Tromsø and on Svalbard, which together covered 62°– 80° MLAT at 290 km altitude during the first five days of the storm, listed as D1–D5. Additionally, the AMPERE data was utilized to identify regions of upward and downward FACs. The main goal was to study the plasma density variations during such a moderate storm and the role of ion-neutral frictional heating in electron density depletions. We summarize the main findings as follows.

1. Increases and depletions of electron density were found. Increases in the polar cap occurred due to PCPs originating from the dayside, in the auroral oval because of soft auroral precipitation, and on the dayside near noon possibly by plasma transport from lower latitudes and cusp precipitation.
2. Electron density depletions were the dominant feature at *F*-region heights outside of the regions of soft auroral precipitation and PCPs, and they lasted at least 5 days. Using EISCAT ion temperature and ion velocity data, we showed that a local ion-frictional heating was observed roughly in 50% of the depleted regions when 200 K was used as the temperature increase limit, raising to 60%−70% as 100 K limit was used. For the rest of depletions, we suggest that the mechanism is neutral composition changes due to ion-neutral frictional heating transported horizontally by neutral winds.
3. Depletions were found in the following two major regions. In the afternoon-evening sector (12–21 MLT) the depleted region was 10°–18° MLAT in width, with the largest latitudinal extent typically in the afternoon sector spanning all measured latitudes 62°–80° MLAT and reaching daily minimum values of −45%−−80%. The second region was located in the morning to pre-noon sector (04–10 MLT), where the ΔN_e depletion minimum ranged between −50% and −60% and occurred at higher latitudes from 72° to 80° MLAT within the auroral oval and partially extending to the polar cap.
4. Even though *F*-region depletions could occur within any of the large-scale FAC regions or outside of them, the downward FAC regions (R2 in the afternoon and evening, R0 in the afternoon, and R1 in the morning) were favored, suggesting that downward currents carried by upward moving ionospheric electrons may provide a small additional effect for depletion.
5. The storm-time trough region occurred within ion frictional heating region in the afternoon-evening sector. The deepening of the trough at lower latitudes was possibly associated with an additional effect from strong ion flows within the SAPS region.

Data Availability Statement

EISCAT data are available for download from https://portal.eiscat.se/schedule/. Omni 2 data link https://omniweb.gsfc.nasa.gov/html/ow_data.html. AMPERE data can be found in https://ampere.jhuapl.edu/download/. IMAGE network data can be downloaded from https://space.fmi.fi/image/www/index.php?page=user_defined. IRI-16 model Python package https://pypi.org/project/iri2016/.

Acknowledgments
This work was supported by the International Space Science Institute (ISSI) in Bern, through ISSI International Team project #487 and Research Council of Finland projects 348782 and 354521. A part of the work of S.-I. Oyama was supported by JSPS KAKENHI 21KK0059, 21H04518, 22K21345, 22H00173, 23K22554, and was carried out by the joint research program of Planetary Plasma and Atmospheric Research Center, Tohoku University. A. Maute was supported by NASA award 80NSSC20K1784. The authors acknowledge the EISCAT Association for the ISR data used in this study. EISCAT is an international association supported by research organizations in China (CRIRP), Finland (SA), Japan (NIPR and ISEE), Norway (NFR), Sweden (VR), and the United Kingdom (UKRI). We acknowledge use of NASA/GSFC's Space Physics Data Facility's CDAWeb service and OMNI data for providing magnetic indices and solar wind parameters. We thank the institutes who maintain the IMAGE Magnetometer Array: Tromsø Geophysical Observatory of UiT the Arctic University of Norway (Norway), Finnish Meteorological Institute (Finland), Institute of Geophysics Polish Academy of Sciences (Poland), GFZ German Research Centre for Geosciences (Germany), Geological Survey of Sweden (Sweden), Swedish Institute of Space Physics (Sweden), Sodankylä Geophysical Observatory of the University of Oulu (Finland), DTU Technical University of Denmark (Denmark), and Science Institute of the University of Iceland (Iceland). The provisioning of data from AAL, GOT, HAS, NRA, VXJ, FKP, ROE, BFE, BOR, HOV, SCO, KUL, and NAQ is supported by the ESA contracts number 4000128139/19/D/CT as well as 4000138064/22/D/KS. We thank the AMPERE team and the AMPERE Science Data Center for providing data products derived from the Iridium Communications constellation, enabled by support from the National Science Foundation.

References

Aa, E., Zhang, S. R., Erickson, P. J., Coster, A. J., Goncharenko, L. P., Varney, R. H., & Eastes, R. (2021). Salient midlatitude ionosphere-thermosphere disturbances associated with SAPS during a minor but geo-effective storm at deep solar minimum. *Journal of Geophysical Research: Space Physics*, *126*(7), e2021JA029509. https://doi.org/10.1029/2021JA029509

Aa, E., Zou, S., Erickson, P. J., Zhang, S. R., & Liu, S. (2020). Statistical analysis of the main ionospheric trough using Swarm in situ measurements. *Journal of Geophysical Research: Space Physics*, *125*(3), e2019JA027583. https://doi.org/10.1029/2019JA027583

Aikio, A. T., Lakkala, T., Kozlovsky, A., & Williams, P. J. (2002). Electric fields and currents of stable drifting auroral arcs in the evening sector. *Journal of Geophysical Research*, *107*(A12), SIA 3-1–SIA 3-14. https://doi.org/10.1029/2001JA009172

Aikio, A. T., Mursula, K., Buchert, S., Forme, F., Amm, O., Marklund, G., et al. (2004). Temporal evolution of two auroral arcs as measured by the Cluster satellite and coordinated ground-based instruments. *Annales Geophysicae*, *22*(12), 4089–4101. https://doi.org/10.5194/ANGEO-22-4089-2004

Aikio, A. T., Pitkänen, T., Kozlovsky, A., & Amm, O. (2006). Method to locate the polar cap boundary in the nightside ionosphere and application to a substorm event. *Annales Geophysicae*, *24*(7), 1905–1917. https://doi.org/10.5194/angeo-24-1905-2006

Akasofu, S. I. (1981). Energy coupling between the solar wind and the magnetosphere. *Space Science Reviews*, *28*(2), 121–190. https://doi.org/10.1007/BF00218810

Amm, O., & Viljanen, A. (1999). Ionospheric disturbance magnetic field continuation from the ground to the ionosphere using spherical elementary current systems. *Earth, Planets and Space*, *51*(6), 431–440. https://doi.org/10.1186/BF03352247/METRICS

Anderson, B. J., Korth, H., Waters, C. L., Green, D. L., Merkin, V. G., Barnes, R. J., & Dyrud, L. P. (2014). Development of large-scale Birkeland currents determined from the Active Magnetosphere and Planetary Electrodynamics Response Experiment. *Geophysical Research Letters*, *41*(9), 3017–3025. https://doi.org/10.1002/2014GL059941

Anderson, B. J., Takahashi, K., & Toth, B. A. (2000). Sensing global Birkeland currents with iridium engineering magnetometer data. *Geophysical Research Letters*, *27*(24), 4045–4048. https://doi.org/10.1029/2000GL000094

Anderson, D. N., Buchau, J., & Heelis, R. A. (1988). Origin of density enhancements in the winter polar cap ionosphere. *Radio Science*, *23*(4), 513–519. https://doi.org/10.1029/RS023i004p00513

Anderson, P. C., Johnston, W. R., & Goldstein, J. (2008). Observations of the ionospheric projection of the plasmapause. *Geophysical Research Letters*, *35*(15), L15110. https://doi.org/10.1029/2008GL033978

Belcher, J. W., & Davis, L. (1971). Large-amplitude Alfvén waves in the interplanetary medium, 2. *Journal of Geophysical Research*, *76*(16), 3534–3563. https://doi.org/10.1029/JA076I016P03534

Bilitza, D. (2001). International reference ionosphere 2000. *Radio Science*, *36*(2), 261–275. https://doi.org/10.1029/2000RS002432

Bilitza, D., Altadill, D., Truhlik, V., Shubin, V., Galkin, I., Reinisch, B., & Huang, X. (2017). International reference ionosphere 2016: From ionospheric climate to real-time weather predictions. *Space Weather*, *15*(2), 418–429. https://doi.org/10.1002/2016SW001593

Bilitza, D., Altadill, D., Zhang, Y., Mertens, C., Truhlik, V., Richards, P., et al. (2014). The international reference ionosphere 2012 – A model of international collaboration. *Journal of Space Weather and Space Climate*, *4*, A07. https://doi.org/10.1051/SWSC/2014004

Bjoland, L. M., Ogawa, Y., Løvhaug, U. P., Lorentzen, D. A., Hatch, S. M., & Oksavik, K. (2021). Electron density depletion region observed in the polar cap ionosphere. *Journal of Geophysical Research: Space Physics*, *126*(1), e2020JA028432. https://doi.org/10.1029/2020JA028432

Borovsky, J. E., & Denton, M. H. (2006). Differences between CME-driven storms and CIR-driven storms. *Journal of Geophysical Research*, *111*(A7), A07S08. https://doi.org/10.1029/2005JA011447

Bristow, W. A., & Jensen, P. (2007). A superposed epoch study of SuperDARN convection observations during substorms. *Journal of Geophysical Research*, *112*(A6), A06232. https://doi.org/10.1029/2006JA012049

Buonsanto, M. J. (1999). Ionospheric storms - A review. *Space Science Reviews*, *88*(3/4), 563–601. https://doi.org/10.1023/A:1005107532631

Buresova, D., Lastovicka, J., Hejda, P., & Bochnicek, J. (2014). Ionospheric disturbances under low solar activity conditions. *Advances in Space Research*, *54*(2), 185–196. https://doi.org/10.1016/J.ASR.2014.04.007

Burns, A. G., Killeen, T. L., & Roble, R. G. (1991). A theoretical study of thermospheric composition perturbations during an impulsive geomagnetic storm. *Journal of Geophysical Research*, *96*(A8), 14153–14167. https://doi.org/10.1029/91JA00678

Burns, A. G., Solomon, S. C., Qian, L., Wang, W., Emery, B. A., Wiltberger, M., & Weimer, D. R. (2012). The effects of corotating interaction region/high speed stream storms on the thermosphere and ionosphere during the last solar minimum. *Journal of Atmospheric and Solar-Terrestrial Physics*, *83*, 79–87. https://doi.org/10.1016/J.JASTP.2012.02.006

Cai, L., Aikio, A., Oyama, S., Ivchenko, N., Vanhamäki, H., Virtanen, I., et al. (2024). Effect of polar cap patches on the high-latitude upper thermospheric winds. *Journal of Geophysical Research: Space Physics*, *129*(8), e2024JA032819. https://doi.org/10.1029/2024JA032819

Cai, L., Oyama, S., Aikio, A., Vanhamäki, H., & Virtanen, I. (2019). Fabry-Perot interferometer observations of thermospheric horizontal winds during magnetospheric substorms. *Journal of Geophysical Research: Space Physics*, *124*(5), 3709–3728. https://doi.org/10.1029/2018JA026241

Carlson, H. C. (2012). Sharpening our thinking about polar cap ionospheric patch morphology, research, and mitigation techniques. *Radio Science*, *47*(4), RS0L21. https://doi.org/10.1029/2011RS004946

Carpenter, D. L., & Lemaire, J. (2004). The plasmasphere boundary layer. *Annales Geophysicae*, *22*(12), 4291–4298. https://doi.org/10.5194/ANGEO-22-4291-2004

Clausen, L. B., Baker, J. B., Ruohoniemi, J. M., Milan, S. E., & Anderson, B. J. (2012). Dynamics of the region 1 Birkeland current oval derived from the Active Magnetosphere and Planetary Electrodynamics Response Experiment (AMPERE). *Journal of Geophysical Research*, *117*(A6), A06233. https://doi.org/10.1029/2012JA017666

Clausen, L. B., H. Baker, J., Ruohoniemi, J. M., Milan, S. E., Coxon, J., Wing, S., et al. (2013). Temporal and spatial dynamics of the regions 1 and 2 Birkeland currents during substorms. *Journal of Geophysical Research: Space Physics*, *118*(6), 3007–3016. https://doi.org/10.1002/jgra.50288

Cowley, S. W. (2000). Magnetosphere-ionosphere interactions: A tutorial review. *Geophysical Monograph Series*, *118*, 91–106. https://doi.org/10.1029/GM118P0091

Crowley, G. (1996). Critical review of ionospheric patches and blobs. *Review of Radio Science*, *619*.

Crowley, G., Hackert, C., Meier, R., Strickland, D., Paxton, L., Pi, X., et al. (2006). Global thermosphere-ionosphere response to onset of 20 November 2003 magnetic storm. *Journal of Geophysical Research*, *111*(A10), A10S18. https://doi.org/10.1029/2005JA011518

Crowley, G., Reynolds, A., Thayer, J. P., Lei, J., Paxton, L. J., Christensen, A. B., et al. (2008). Periodic modulations in thermospheric composition by solar wind high speed streams. *Geophysical Research Letters*, *35*(21), L21106. https://doi.org/10.1029/2008GL035745

Deminov, M., & Shubin, V. (2018). Empirical model of the location of the main ionospheric trough. *Geomagnetism and Aeronomy*, *58*(3), 348–355. https://doi.org/10.1134/S0016793218030064

Deng, Y., & Ridley, A. J. (2006). Role of vertical ion convection in the high-latitude ionospheric plasma distribution. *Journal of Geophysical Research*, *111*(A9), A09314. https://doi.org/10.1029/2006JA011637

Denton, M. H., & Borovsky, J. E. (2012). Magnetosphere response to high-speed solar wind streams: A comparison of weak and strong driving and the importance of extended periods of fast solar wind. *Journal of Geophysical Research*, *117*(A9), A00L05. https://doi.org/10.1029/2011JA017124

Denton, M. H., Ulich, T., & Turunen, E. (2009). Modification of midlatitude ionospheric parameters in the F_2 layer by persistent high-speed solar wind streams. *Space Weather*, *7*(4), S04006. https://doi.org/10.1029/2008SW000443

Doe, R. A., Mendillo, M., Vickrey, J. F., Zanetti, L. J., & Eastes, R. W. (1993). Observations of nightside auroral cavities. *Journal of Geophysical Research*, *98*(A1), 293–310. https://doi.org/10.1029/92JA02004

Doe, R. A., Vickrey, J. F., & Mendillo, M. (1995). Electrodynamic model for the formation of auroral ionospheric cavities. *Journal of Geophysical Research*, *100*(A6), 9683–9696. https://doi.org/10.1029/95JA00001

Emelyanov, L. Y., Katsko, S. V., Lyashenko, M. V., & Chernogor, L. F. (2023). Ionosphere response to geospace storm on 25 September 2016 over Kharkiv (Ukraine). *Advances in Space Research*, *71*(8), 3323–3345. https://doi.org/10.1016/j.asr.2023.02.004

Fang, X., Randall, C. E., Lummerzheim, D., Wang, W., Lu, G., Solomon, S. C., & Frahm, R. A. (2010). Parameterization of monoenergetic electron impact ionization. *Geophysical Research Letters*, *37*(22), L22106. https://doi.org/10.1029/2010GL045406

Forbes, J. M. (2007). Dynamics of the thermosphere. *Journal of the Meteorological Society of Japan. Ser. II*, *85*, 193–213. https://doi.org/10.2151/jmsj.85B.193

Foster, J. C., & Burke, W. J. (2002). SAPS: A new categorization for sub-auroral electric fields. *Eos*, *83*(36), 393–394. https://doi.org/10.1029/2002EO000289

Foster, J. C., Coster, A. J., Erickson, P. J., Holt, J. M., Lind, F. D., Rideout, W., et al. (2005). Multiradar observations of the polar tongue of ionization. *Journal of Geophysical Research*, *110*(A9), A09S31. https://doi.org/10.1029/2004JA010928

Fuller-Rowell, T., Codrescu, M., Moffett, R., & Quegan, S. (1994). Response of the thermosphere and ionosphere to geomagnetic storms. *Journal of Geophysical Research*, *99*(A3), 3893–3914. https://doi.org/10.1029/93JA02015

Gonzalez, W. D., Joselyn, J. A., Kamide, Y., Kroehl, H. W., Rostoker, G., Tsurutani, B. T., & Vasyliunas, V. M. (1994). What is a geomagnetic storm? *Journal of Geophysical Research*, *99*(A4), 5771–5792. https://doi.org/10.1029/93JA02867

Gonzalez, W. D., Tsurutani, B. T., & Gonzalez, A. L. C. D. (1999). Interplanetary origin of geomagnetic storms. *Space Science Reviews*, *88*, 529–562. https://doi.org/10.1023/A:1005160129098

Gosling, J. T., & Pizzo, V. J. (1999). Formation and evolution of corotating interaction regions and their three dimensional structure. *Space Science Reviews*, *89*, 21–52. https://doi.org/10.1023/A:1005291711900/METRICS

Grandin, M., Aikio, A., Kozlovsky, A., Ulich, T., & Raita, T. (2015). Effects of solar wind high-speed streams on the high-latitude ionosphere: Superposed epoch study. *Journal of Geophysical Research: Space Physics*, *120*(12), 10–669. https://doi.org/10.1002/2015JA021785

Grandin, M., Aikio, A., Kozlovsky, A., Ulich, T., & Raita, T. (2017). Cosmic radio noise absorption in the high-latitude ionosphere during solar wind high-speed streams. *Journal of Geophysical Research: Space Physics*, *122*(5), 5203–5223. https://doi.org/10.1002/2017JA023923

Grandin, M., Aikio, A. T., & Kozlovsky, A. (2019). Properties and geoeffectiveness of solar wind high-speed streams and stream interaction regions during solar cycles 23 and 24. *Journal of Geophysical Research: Space Physics*, *124*(6), 3871–3892. https://doi.org/10.1029/2018JA026396

Heppner, J. P., & Maynard, N. C. (1987). Empirical high-latitude electric field models. *Journal of Geophysical Research*, *92*(A5), 4467–4489. https://doi.org/10.1029/JA092iA05p04467

Hosokawa, K., Zou, Y., & Nishimura, Y. (2019). Airglow patches in the polar cap region: A review. *Space Science Reviews*, *215*(8), 1–17. https://doi.org/10.1007/s11214-019-0616-8

Iijima, T., & Potemra, T. A. (1976). Field-aligned currents in the dayside cusp observed by triad. *Journal of Geophysical Research*, *81*(34), 5971–5979. https://doi.org/10.1029/JA081i034p05971

Iijima, T., & Potemra, T. A. (1978). Large-scale characteristics of field-aligned currents associated with substorms. *Journal of Geophysical Research*, *83*(A2), 599–615. https://doi.org/10.1029/JA083IA02P00599

Iijima, T., & Potemra, T. A. (1982). The relationship between interplanetary quantities and Birkeland current densities. *Geophysical Research Letters*, *9*(4), 442–445. https://doi.org/10.1029/GL009i004p00442

Iyemori, T., Takeda, M., Nose, M., Odagi, Y., & Toh, H. (2010). *Mid-latitude geomagnetic indices "ASY" and "SYM" for 2009 (provisional)*. Data Analysis Center for Geomagnetism and Space Magnetism, Graduate School of Science, Kyoto University. https://doi.org/10.14989/267216

Jayachandran, P., MacDougall, J., Donovan, E., Ruohoniemi, J., Liou, K., Moorcroft, D., & St-Maurice, J.-P. (2003). Substorm associated changes in the high-latitude ionospheric convection. *Geophysical Research Letters*, *30*(20), 2064. https://doi.org/10.1029/2003GL017497

Juusola, L., Milan, S. E., Lester, M., Grocott, A., & Imber, S. M. (2014). Interplanetary magnetic field control of the ionospheric field-aligned current and convection distributions. *Journal of Geophysical Research: Space Physics*, *119*(4), 3130–3149. https://doi.org/10.1002/2013JA019455

Kamide, Y., & Vickrey, J. F. (1983). Relative contribution of ionospheric conductivity and electric field to the auroral electrojets. *Journal of Geophysical Research*, *88*(A10), 7989–7996. https://doi.org/10.1029/JA088iA10p07989

Kamide, Y., Yokoyama, N., Gonzalez, W., Tsurutani, B. T., Daglis, I. A., Brekke, A., & Masuda, S. (1998). Two-step development of geomagnetic storms. *Journal of Geophysical Research*, *103*(A4), 6917–6921. https://doi.org/10.1029/97JA03337

Karlsson, T., & Marklund, G. (1998). Simulations of effects of small-scale auroral current closure in the return current region. *Physics of Space Plasmas*, *15*, 401.

Kauristie, K., Pulkkinen, T. I., Pellinen, R. J., & Opgenoorth, H. J. (1996). What can we tell about global auroral-electrojet activity from a single meridional magnetometer chain? *Annales Geophysicae*, *14*(11), 1177–1185. https://doi.org/10.1007/s00585-996-1177-1

Kilpua, E., Koskinen, H. E., & Pulkkinen, T. I. (2017). Coronal mass ejections and their sheath regions in interplanetary space. *Living Reviews in Solar Physics*, *14*(1), 5. https://doi.org/10.1007/S41116-017-0009-6

King, J. H., & Papitashvili, N. E. (2005). Solar wind spatial scales in and comparisons of hourly wind and ace plasma and magnetic field data. *Journal of Geophysical Research*, *110*(A2), A02104. https://doi.org/10.1029/2004JA010649

Laundal, K. M., Gjerloev, J. W., Østgaard, N., Reistad, J. P., Haaland, S., Snekvik, K., et al. (2016). The impact of sunlight on high-latitude equivalent currents. *Journal of Geophysical Research: Space Physics*, *121*(3), 2715–2726. https://doi.org/10.1002/2015JA022236

Lei, J., Thayer, J. P., Forbes, J. M., Wu, Q., She, C., Wan, W., & Wang, W. (2008). Ionosphere response to solar wind high-speed streams. *Geophysical Research Letters*, *35*(19), L19105. https://doi.org/10.1029/2008GL035208

Liu, J., Liu, L., Zhao, B., Lei, J., Thayer, J. P., & McPherron, R. L. (2012). Superposed epoch analyses of thermospheric response to CIRs: Solar cycle and seasonal dependencies. *Journal of Geophysical Research*, *117*(A9), A00L10. https://doi.org/10.1029/2011JA017315

Lockwood, M., & Carlson, H. C., Jr. (1992). Production of polar cap electron density patches by transient magnetopause reconnection. *Geophysical Research Letters*, *19*(17), 1731–1734. https://doi.org/10.1029/92GL01993

Marchaudon, A., Blelly, P.-L., Grandin, M., Aikio, A., Kozlovsky, A., & Virtanen, I. (2018). IPIM modeling of the ionospheric *F*2 layer depletion at high latitudes during a high-speed stream event. *Journal of Geophysical Research: Space Physics*, *123*(8), 7051–7066. https://doi.org/10.1029/2018JA025744

Marklund, G. T., Ivchenko, N., Karlsson, T., Fazakerley, A., Dunlop, M., Lindqvist, P. A., et al. (2001). Temporal evolution of the electric field accelerating electrons away from the auroral ionosphere. *Nature*, *414*(6865), 724–727. https://doi.org/10.1038/414724A

Mayer, H. G., Harris, I., & Spencer, N. W. (1978). Some properties of upper atmosphere dynamics. *Reviews of Geophysics*, *16*(4), 539–565. https://doi.org/10.1029/RG016I004P00539

Meier, R., Crowley, G., Strickland, D., Christensen, A., Paxton, L., Morrison, D., & Hackert, C. (2005). First look at the 20 November 2003 superstorm with TIMED/GUVI: Comparisons with a thermospheric global circulation model. *Journal of Geophysical Research*, *110*(A9), A09S41. https://doi.org/10.1029/2004JA010990

Moen, J., Carlson, H., Oksavik, K., Nielsen, C., Pryse, S., Middleton, H., et al. (2006). EISCAT observations of plasma patches at sub-auroral cusp latitudes. *Annales Geophysicae*, *24*(9), 2363–2374. https://doi.org/10.5194/angeo-24-2363-2006

Nilsson, H., Sergienko, T. I., Ebihara, Y., & Yamauchi, M. (2005). Quiet-time mid-latitude trough: Influence of convection, field-aligned currents and proton precipitation. *Annales Geophysicae*, *23*(10), 3277–3288. https://doi.org/10.5194/ANGEO-23-3277-2005

Østgaard, N., Moen, J., Mende, S., Frey, H., Immel, T., Gallop, P., et al. (2005). Estimates of magnetotail reconnection rate based on IMAGE FUV and EISCAT measurements. *Annales Geophysicae*, *23*(1), 123–134. https://doi.org/10.5194/angeo-23-123-2005,2005

Oyama, S., Hosokawa, K., Vanhamäki, H., Aikio, A., Sakanoi, T., Cai, L., et al. (2023). IMF dependence of midnight bifurcation in the thermospheric wind at an auroral latitude based on nine winter measurements in Tromsø, Norway. *Geophysical Research Letters*, *50*(14), e2023GL104334. https://doi.org/10.1029/2023GL104334

Pedatella, N. M. (2016). Impact of the lower atmosphere on the ionosphere response to a geomagnetic superstorm. *Geophysical Research Letters*, *43*(18), 9383–9389. https://doi.org/10.1002/2016GL070592

Pedatella, N. M., & Liu, H.-L. (2018). The influence of internal atmospheric variability on the ionosphere response to a geomagnetic storm. *Geophysical Research Letters*, *45*(10), 4578–4585. https://doi.org/10.1029/2018GL077867

Pedersen, M. N., Vanhamäki, H., Aikio, A. T., Käki, S., Workayehu, A. B., Waters, C. L., & Gjerloev, J. W. (2021). Field-aligned and ionospheric currents by AMPERE and SuperMAG during HSS/SIR-driven storms. *Journal of Geophysical Research: Space Physics*, *126*(11), e2021JA029437. https://doi.org/10.1029/2021JA029437

Pedersen, M. N., Vanhamäki, H., Aikio, A. T., Waters, C. L., Gjerloev, J. W., Käki, S., & Workayehu, A. B. (2022). Effect of ICME-driven storms on field-aligned and ionospheric currents from AMPERE and SuperMAG. *Journal of Geophysical Research: Space Physics*, *127*(8), e2022JA030423. https://doi.org/10.1029/2022JA030423

Pierrard, V., & Voiculescu, M. (2011). The 3D model of the plasmasphere coupled to the ionosphere. *Geophysical Research Letters*, *38*(12), L12104. https://doi.org/10.1029/2011GL047767

Prölss, G. (1997). Magnetic storm associated perturbations of the upper atmosphere. *Geophysical Monograph Series*, *98*, 227–241. https://doi.org/10.1029/gm098p0227

Prölss, G. (2007). The equatorward wall of the subauroral trough in the afternoon/evening sector. *Annales Geophysicae*, *25*(3), 645–659. https://doi.org/10.5194/angeo-25-645-2007

Pryse, S. E., Kersley, L., Williams, M. J., & Walker, I. K. (1998). The spatial structure of the dayside ionospheric trough. *Annales Geophysicae*, *16*(10), 1169–1179. https://doi.org/10.1007/S00585-998-1169-4

Richards, P. G., & Voglozin, D. (2011). Reexamination of ionospheric photochemistry. *Journal of Geophysical Research*, *116*(A8), A08307. https://doi.org/10.1029/2011JA016613

Richardson, I. G. (2018). Solar wind stream interaction regions throughout the heliosphere. *Living Reviews in Solar Physics*, *15*(1), 1. https://doi.org/10.1007/s41116-017-0011-z

Rietveld, M., Wright, J., Zabotin, N., & Pitteway, M. (2008). The Tromsø dynasonde. *Polar Science*, *2*(1), 55–71. https://doi.org/10.1016/j.polar.2008.02.001

Rodger, A. S. (2008). The mid-latitude trough—Revisited. *Geophysical Monograph Series*, *181*, 25–33. https://doi.org/10.1029/181GM04

Rodger, A. S., Moffett, R. J., & Quegan, S. (1992). The role of ion drift in the formation of ionisation troughs in the mid- and high-latitude ionosphere-a review. *Journal of Atmospheric and Terrestrial Physics*, *54*, 1–30. https://doi.org/10.1016/0021-9169(92)90082-V

Ruohoniemi, J. M., & Greenwald, R. A. (1996). Statistical patterns of high-latitude convection obtained from Goose Bay HF radar observations. *Journal of Geophysical Research*, *101*(A10), 21743–21763. https://doi.org/10.1029/96JA01584

Schmölter, E., & Berdermann, J. (2021). Predicting the effects of solar storms on the ionosphere based on a comparison of real-time solar wind data with the best-fitting historical storm event. *Atmosphere*, *12*(12), 1684. https://doi.org/10.3390/atmos12121684

Schunk, R. W., Banks, P. M., & Raitt, W. J. (1976). Effects of electric fields and other processes upon the nighttime high-latitude *F* layer. *Journal of Geophysical Research*, *81*(19), 3271–3282. https://doi.org/10.1029/JA081i019p03271

Schunk, R. W., & Nagy, A. F. (1980). Ionospheres of the terrestrial planets. *Reviews of Geophysics*, *18*(4), 813–852. https://doi.org/10.1029/RG018I004P00813

Shepherd, S. G. (2014). Altitude-adjusted corrected geomagnetic coordinates: Definition and functional approximations. *Journal of Geophysical Research: Space Physics*, *119*(9), 7501–7521. https://doi.org/10.1002/2014JA020264

Shinbori, A., Otsuka, Y., Tsugawa, T., Nishioka, M., Kumamoto, A., Tsuchiya, F., et al. (2018). Temporal and spatial variations of storm time midlatitude ionospheric trough based on global GNSS-TEC and Arase satellite observations. *Geophysical Research Letters*, *45*(15), 7362–7370. https://doi.org/10.1029/2018GL078723

Sojka, J. J., McPherron, R. L., Eyken, A. P. V., Nicolls, M. J., Heinselman, C. J., & Kelly, J. D. (2009). Observations of ionospheric heating during the passage of solar coronal hole fast streams. *Geophysical Research Letters*, *36*(19), L19105. https://doi.org/10.1029/2009GL039064

Spiro, R., Heelis, R., & Hanson, W. (1979). Rapid subauroral ion drifts observed by Atmosphere Explorer C. *Geophysical Research Letters*, *6*(8), 657–660. https://doi.org/10.1029/GL006i008p00657

St.-Maurice, J.-P., & Laneville, P. J. (1998). Reaction rate of O^+ with O_2, N_2, and no under highly disturbed auroral conditions. *Journal of Geophysical Research*, *103*(A8), 17519–17521. https://doi.org/10.1029/98JA01387

Tanskanen, E. (2009). A comprehensive high-throughput analysis of substorms observed by IMAGE magnetometer network: Years 1993–2003 examined. *Journal of Geophysical Research*, *114*(A5), A05204. https://doi.org/10.1029/2008JA013682

Thayer, J. P., Lei, J., Forbes, J. M., Sutton, E. K., & Nerem, R. S. (2008). Thermospheric density oscillations due to periodic solar wind highspeed streams. *Journal of Geophysical Research*, *113*(A6), A06307. https://doi.org/10.1029/2008JA013190

Thomas, E. G., & Shepherd, S. G. (2018). Statistical patterns of ionospheric convection derived from mid-latitude, high-latitude, and polar SuperDARN HF radar observations. *Journal of Geophysical Research: Space Physics*, *123*(4), 3196–3216. https://doi.org/10.1002/2018JA025280

Tsurutani, B. T., & Gonzalez, W. D. (1987). The cause of high-intensity long-duration continuous AE activity (HILDCAAs): Interplanetary Alfvén wave trains. *Planetary and Space Science*, *35*(4), 405–412. https://doi.org/10.1016/0032-0633(87)90097-3

Tsurutani, B. T., Gonzalez, W. D., Gonzalez, A. L., Guarnieri, F. L., Gopalswamy, N., Grande, M., et al. (2006). Corotating solar wind streams and recurrent geomagnetic activity: A review. *Journal of Geophysical Research*, *111*(A7), A07S01. https://doi.org/10.1029/2005JA011273

Tsurutani, B. T., Gonzalez, W. D., Guarnieri, F., Kamide, Y., Zhou, X., & Arballo, J. K. (2004). Are high-intensity long-duration continuous AE activity (HILDCAA) events substorm expansion events? *Journal of Atmospheric and Solar-Terrestrial Physics*, *66*(2), 167–176. https://doi.org/10.1016/j.jastp.2003.08.015

Tsurutani, B. T., Ho, C. M., Smith, E. J., Neugebauer, M., Goldstein, B. E., Mok, J. S., et al. (1994). The relationship between interplanetary discontinuities and Alfvén waves: Ulysses observations. *Geophysical Research Letters*, *21*, 2267–2270. https://doi.org/10.1029/94GL02194

Tsurutani, B. T., & Smith, E. J. (1979). Interplanetary discontinuities: Temporal variations and the radial gradient from 1 to 8.5 au. *Journal of Geophysical Research*, *84*(A6), 2773–2787. https://doi.org/10.1029/JA084IA06P02773

Turner, N. E., Cramer, W. D., Earles, S. K., & Emery, B. A. (2009). Geoefficiency and energy partitioning in CIR-driven and CME-driven storms. *Journal of Atmospheric and Solar-Terrestrial Physics*, *71*(10–11), 1023–1031. https://doi.org/10.1016/J.JASTP.2009.02.005

Vanhamäki, H., & Juusola, L. (2020). Introduction to spherical elementary current systems. In M. W. Dunlop & H. Lühr (Eds.), *Ionospheric multi-spacecraft analysis tools: Approaches for deriving ionospheric parameters* (pp. 5–33). Springer International Publishing. https://doi.org/10.1007/978-3-030-26732-2_2

Verkhoglyadova, O. P., Tsurutani, B. T., Mannucci, A. J., Mlynczak, M. G., Hunt, L. A., & Runge, T. (2013). Variability of ionospheric tec during solar and geomagnetic minima (2008 and 2009): External high speed stream drivers. *Annales Geophysicae*, *31*(2), 263–276. https://doi.org/10.5194/ANGEO-31-263-2013

Voiculescu, M., Nygrén, T., Aikio, A. T., Vanhamäki, H., & Pierrard, V. (2016). Postmidnight ionospheric troughs in summer at high latitudes. *Journal of Geophysical Research: Space Physics*, *121*(12), 12171–12185. https://doi.org/10.1002/2016JA023360

Voiculescu, M., Nygrn, T., Aikio, A., & Kuula, R. (2010). An olden but golden EISCAT observation of a quiet-time ionospheric trough. *Journal of Geophysical Research*, *115*(A10), A10315. https://doi.org/10.1029/2010JA015557

Weimer, D. R. (2001). Maps of ionospheric field-aligned currents as a function of the interplanetary magnetic field derived from Dynamics Explorer 2 data. *Journal of Geophysical Research*, *106*(A7), 12889–12902. https://doi.org/10.1029/2000JA000295

Whalen, J. A. (1989). The daytime *F* layer trough and its relation to ionospheric-magnetospheric convection. *Journal of Geophysical Research*, *94*, 17169–17184. https://doi.org/10.1029/JA094IA12P17169

Yang, N., Le, H., & Liu, L. (2015). Statistical analysis of ionospheric mid-latitude trough over the Northern Hemisphere derived from GPS total electron content data. *Earth, Planets and Space*, *67*, 1–11. https://doi.org/10.1186/s40623-015-0365-1

Yang, N., Le, H., & Liu, L. (2016). Statistical analysis of the mid-latitude trough position during different categories of magnetic storms and different storm intensities. *Earth, Planets and Space*, *68*(1), 1–11. https://doi.org/10.1186/s40623-016-0554-6

Yokoyama, N., & Kamide, Y. (1997). Statistical nature of geomagnetic storms. *Journal of Geophysical Research*, *102*(A7), 14215–14222. https://doi.org/10.1029/97JA00903

Zettergren, M., Lynch, K., Hampton, D., Nicolls, M., Wright, B., Conde, M., et al. (2014). Auroral ionospheric *F* region density cavity formation and evolution: MICA campaign results. *Journal of Geophysical Research: Space Physics*, *119*(4), 3162–3178. https://doi.org/10.1002/2013JA019583

Zettergren, M., & Semeter, J. (2012). Ionospheric plasma transport and loss in auroral downward current regions. *Journal of Geophysical Research*, *117*(A6), A06306. https://doi.org/10.1029/2012JA017637

Zhang, Y., Paxton, L. J., Morrison, D., Wolven, B., Kil, H., Meng, C. I., et al. (2004). O/N_2 changes during 1–4 October 2002 storms: Image SI-13 and TIMED/GUVI observations. *Journal of Geophysical Research*, *109*(A10), A10308. https://doi.org/10.1029/2004JA010441